Case study of outer radiation belt electron precipitation inferred from balloon-observed x-ray spectra

Amanda Nichole Baker

A thesis submitted in partial fulfillment of the
requirements for the degree of

Master of Science

University of Washington

2010

Program Authorized to Offer Degree:
Department of Earth and Space Sciences

University of Washington
Graduate School

This is to certify that I have examined this copy of a master's thesis by

Amanda Nichole Baker

and have found that it is complete and satisfactory in all respects,
and that any and all revisions required by the final
examining committee have been made.

Committee Members:

_____
Michael P. McCarthy

_____
Robert H. Holzworth

_____
Erika M. Harnett

Date:_____

In presenting this thesis in partial fulfillment of the requirements for a master's degree at the University of Washington, I agree that the Library shall make its copies freely available for inspection. I further agree that extensive copying of this thesis is allowable only for scholarly purposes, consistent with "fair use" as prescribed in the U.S. Copyright Law. Any other reproduction for any purposes or by any means shall not be allowed without my written permission.

Signature_____

Date_____

University of Washington

Abstract

Case study of outer radiation belt electron precipitation inferred from balloon-observed x-ray spectra

Amanda Nichole Baker

Chair of the Supervisory Committee:
Michael P. McCarthy, Research Professor
Department of Earth and Space Sciences

First results and analysis are reported for x-ray spectra data collected during the Piggyback test flight of the Balloon Array for RBSP Relativistic Electron Losses (BARREL) platform for measuring radiation belt precipitation. Electron precipitation was observed during a large substorm on February 14th, 2009. The calibrated and background-subtracted bremsstrahlung spectra were temporally characterized by fit parameters using two types of functions, exponential and power law, for lower (90 – 200 keV) and higher energies (1.4 – 8 MeV) respectively. The lower-energy spectra were determined to be a result of substorm activity. Flux increases in the higher-energy spectra were also observed during the substorm activity. Estimates of one parent electron spectrum yielded a non-unique solution. Attempts to limit the possible solutions by comparing precipitating electron measurements from Solar Anomalous and Magnetospheric Particle Explorer (SAMPEX) were unsuccessful. The spectra also revealed two previously unobserved spectral peaks at 350 keV and 4.8 MeV. High-energy protons were

eliminated as a possible source of the peaks. Some of the methods developed to study this test flight dataset and the initial results discovered will serve as a foundation for the analysis of radiation belt losses in the upcoming BARREL campaign.

TABLE OF CONTENTS

LIST OF FIGURES

LIST OF TABLES

Introduction

Earth's magnetic field traps energetic particles in certain regions around the Earth called the radiation belts. The outer radiation belt in particular, is a highly dynamic system, with daily changes in electron flux. While the acceleration processes that increase radiation belt electron flux have been extensively studied, radiation belt loss processes have become a topic of interest over the last decade [*Millan and Thorne*, 2007]. The purpose of this thesis is to analyze temporal and spectral characteristics of indirect observations of radiation belt electron losses and estimate the spectra of the original precipitating electrons. Unlike previous studies, the x-ray energies greater than 1.4 MeV will be analyzed. These results can be correlated with the behavior of other observed phenomena to identify radiation belt loss mechanisms. To provide context for this research, this introduction will provide a short review of particular concepts related to this thesis, as well as a summary of previous work in this area.

The Earth has a complex and intricate space weather system that originates with the Earth's distorted dipole magnetic field. The Earth's magnetic field acts as a shielding system, deflecting away from the surface of the Earth most of the charged particles emitted by the Sun. This shielding system is called the magnetosphere. The main components of the magnetosphere and the space weather system are shown in **Figure 1**. As seen in the figure, the Sun's emitted particles (collectively called the solar wind) flow supersonically from the left towards the Earth's magnetosphere. The yellow arrows in the solar wind indicate that the solar wind is deflected by the outer pressure-balanced boundary of the magnetosphere, the

magnetopause (not shown). Before reaching the magnetopause, the solar wind slows to subsonic speeds starting at the bow shock.

Inside the magnetopause, the white lines going into the Earth in the Northern Hemisphere and coming out of the Earth in the Southern Hemisphere are the magnetic field lines of Earth. The dipole is compressed and stronger on the dayside (side towards the Sun) as well as stretched out on the nightside (side away from the Sun) as a result of the presence of the solar wind. The stretched nightside magnetic field lines form a structure called the magnetotail. Regions of charged particles exist inside the magnetosphere as well. The ionosphere is a layer of the atmosphere where free electrons and ions exist as plasmas and interact with the magnetosphere. Though the figure implies a static magnetic structure, the magnetospheric fields and plasmas are dynamic and in constant motion.

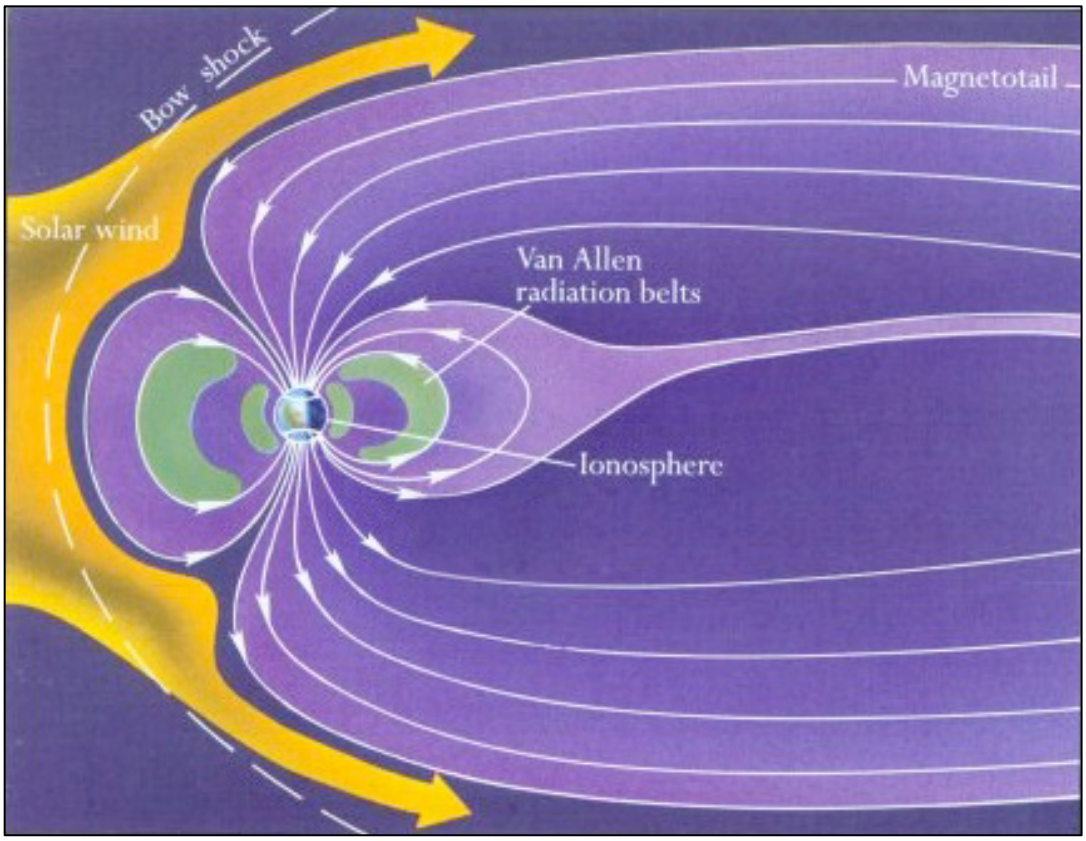

Figure 1. A simplified illustration of the main components of the interactions between the Sun's solar wind and the Earth's magnetic field [*Kaler, J. B.*, 1992].

The green regions in **Figure 1** are the Van Allen radiation belts. Highly energetic particles can become trapped due to forces from the magnetic field in these areas. James Van Allen first discovered the torus-shaped regions in 1958 with measurements from a Geiger tube on the Explorer 1 spacecraft [Van Allen, 1983]. There are two separate radiation belts: the inner and the outer belts. A region of lower energetic particle density known as the slot region separates the belts. The inner radiation belt is between 7,600 km (1.2 Re) and 16,000 km (2.5 Re) away from the center of the Earth. It contains electrons, ions, and highly energetic protons with energies as high as hundreds of Mega electron-volts (MeV). The inner belt is

generated by the interaction of cosmic rays with the atmosphere, creating protons from decaying neutrons. This radiation belt is generally stable, with little or no change in its diameter or particle flux over long time scales [*Li and Temerin*, 2001].

The outer radiation belt is past the slot region and commonly fills a space between 19,000 km (3 Re) and 38,000 km (6 Re) away from the center of the Earth; however, the strength and size of the belt can vary significantly based on geomagnetic activity [*Millan and Thorne*, 2007]. The outer radiation belt consists primarily of electrons with energies between .5 MeV and 10 MeV. Electrons from the solar wind and from the ionosphere are sources of the outer radiation belt particles. The electron energies from these regions, however, are very low compared with the relativistic energies in the outer radiation belt. The solar wind carries electrons with energies of tens of eV, while the ionosphere has electrons of a few eV [*Li and Temerin*, 2001]. These particles therefore undergo acceleration processes to reach relativistic energies. Two examples of the acceleration processes are radial diffusion and wave-particle interactions.

Radial diffusion involves large-scale fluctuating magnetic and electric fields accelerating particles earthward or outward across magnetic "shells" called L-shells [*Kivelson and Russell*, 1995]. This diffusion accelerates the low-energy solar wind or ionospheric electrons to relativistic energies as they enter the radiation belt. Gyro-resonant waves present in the magnetosphere can also interact with electrons, accelerating electrons to higher energies by transfer of kinetic energy [*Chen et al.*, 2007]. This process is a part of wave-particle interactions. The slot region is

formed as a result of a balance between radial diffusion and wave-particle interactions [*Meredith et al.*, 2007].

Radiation belt particles undergo three types of motions from interactions with Earth's magnetic field. These three types of motion are illustrated in **Figure 2**. First, due to the Lorentz force $\left(\vec{F} = q(\vec{v} \times \vec{B})\right)$, a charged particle with some initial velocity perpendicular to a magnetic field line will gyrate around the magnetic field line in the direction determined by its charge.

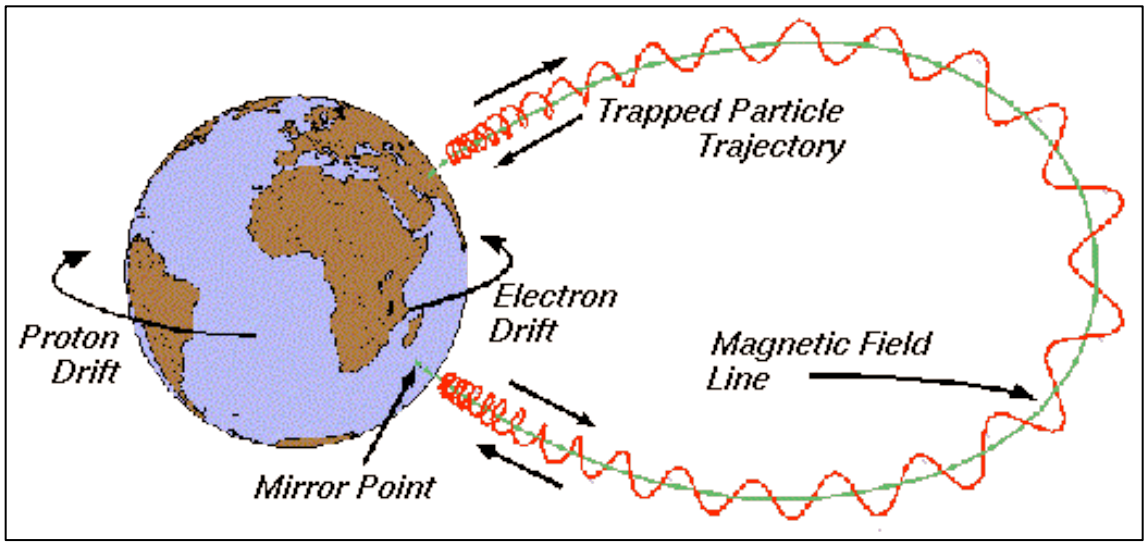

Figure 2. Simple depiction of the motions particles undergo within the radiation belt, including the location of the mirror point [*Baumjohann and Treumann*, 1996].

The second particle motion, bounce motion, is determined by the gradient force ($\vec{F} = -(\vec{\mu} \cdot \nabla)\vec{B}$), where μ is the magnetic moment. The magnetic moment ($\mu = \frac{1/2mv_{\perp}^2}{B}$) is the first adiabatic invariant, which means that the particle's perpendicular energy is proportional to the magnetic field strength. This means

that as the particle travels into regions where the magnetic field is stronger (toward the pole), the perpendicular velocity also increases. The result is a decrease in the parallel velocity until the gradient force reverses the particle back along the field line to travel towards the other pole. This place where the particle is pushed back along the field line is called the mirror point. A single particle undergoes a third motion called drift motion, due to both the curvature $\left(\vec{F} = mv^2 \frac{\vec{R}_c}{R_c^2} \right)$ and the gradient forces.

Research on the outer radiation belt has mainly focused on acceleration processes of electrons, but over the last decade, identifying the loss processes has become a topic of interest. *Reeves et al.* [2003] investigated the total flux of the outer radiation belt during several hundred geomagnetic storms and reported that only 53% of the events showed an increase in trapped electron flux, while 19% showed a decrease, and 28% showed no change. This result illustrates that loss processes are equally as important as acceleration processes to investigate in order to quantify the dynamics of the outer radiation belt.

While all the possible processes of radiation belt losses are not fully understood, one type – electron precipitation – can be quantified and analyzed with the use of instruments onboard high-altitude (~35 km) balloons circumnavigating the poles. Electron precipitation occurs when radiation belt electrons are lost to the atmosphere. If an electron has enough parallel velocity that its mirroring point is inside the atmosphere (at about 100 km altitude), then the electron will most likely

collide with atmospheric neutrals. These collisions can create bremsstrahlung x-rays, which are measured from balloon-borne x-ray detectors.

Electron precipitation is a type of radiation belt loss, but the source mechanisms (the magnetospheric phenomenon that changes the electron's mirroring point) are not fully understood. Balloon measurements of the x-ray bremsstrahlung can be used to help identify dominant radiation belt loss mechanisms. A balloon moves slowly around the polar region, observing the same area over a longer period of time than low-orbiting satellites can. The temporal characteristics of radiation belt losses measured by the balloon can then be quantified and correlated with the behavior of magnetospheric phenomena observed by other platforms. For example, initial onset and amplitude increases in the x-ray spectrum should correspond with onset and amplitude in the proposed phenomenon. Furthermore, the original radiation belt electron spectrum that produced the x-ray bremsstrahlung can be estimated data from the balloon data. The calculated electron energies should resemble the energies that the proposed phenomenon can act upon. Thus balloon observations play a key role in discerning the dynamics of the outer radiation belt.

Bremsstrahlung x-rays were first measured by a balloon-borne detector in 1957 [*Winckler et al.*, 1958], but were thought to originate from the Sun because the radiation belts had not yet been discovered. The correct emission source was identified soon after the belts' discovery. The basic techniques for analyzing bremsstrahlung x-rays were developed in early balloon experiments in the 1960s and have been improved upon in subsequent decades by means of new experiments

with higher temporal and spectral resolution and more sophisticated computer calculations.

Anderson and Enemark [1960] constructed a rough estimate of the original electron spectrum using basic principles of bremsstrahlung production and atmospheric attenuation. The authors noted, however, that the constructed electron spectrum did not accurately reproduce the x-ray spectra for energies greater than 100 keV. *Berger and Seltzer* [1972] greatly improved upon previous work by avoiding simplifications with the use of a Monte Carlo model to calculate bremsstrahlung atmospheric absorption and scattering. The work of *Berger and Seltzer* laid the foundation for most Monte Carlo simulations employed today [*Smith et al*., 1995].

With regards to characterizing the x-ray spectrum, *Barcus and Rosenberg* [1966] fit an exponential function to the x-ray data and characterized the spectra by a fit parameter called the *e*-folding energy (E_0). The *e*-folding energy is the amount of energy required to decrease the flux by $1/e$ of its previous value. This type of characterization, along with power law fitting, is still used today.

Early balloon experiments focused on x-ray energies less than 300 keV [*Millan and Thorne,* 2007]. However, this narrow energy range covered only the lowest electron energies available in the radiation belt. As a result, the observed x-rays represented only a fraction of the possible precipitated x-rays. X-rays from electron precipitation in the MeV range were first observed in 1996 from a germanium spectrometer on a balloon flight in Kiruna, Sweden. *Foat et al.* [1998] reported that the bremsstrahlung x-rays were derived from a mono-energetic beam

of 1.7 MeV precipitating electrons. However, *Foat et al.* also pointed out that the x-ray spectrum observed extended to the 1.4 MeV instrument limit, implying the precipitation could extend out to higher energies.

The MeV Auroral X-ray Imaging and Spectroscopy (MAXIS) and the MINIature Spectrometer (MINIS) were two balloon campaigns following the Kiruna flight that also observed MeV x-rays. MAXIS used the same germanium spectrometer as was on the Kiruna flight, but also only characterized the x-ray spectra up to 1.4 MeV [*Millan et al.*, 2002]. The MINIS balloon observed x-rays over a few hours and *McCarthy et al.* [2005] reported on many spectral peaks within the x-ray data. *McCarthy et al.* reported on x-ray energies up to 6 MeV, but focused on indentifying the source of the spectral peaks. Spectral peaks can be produced by sources other than electron precipitation such as cosmic rays or even the instrument itself. It is important to identify these other spectral characteristics to be sure any analysis of the precipitating electron x-ray spectrum includes only x-rays produced by those electrons.

A test flight for a new balloon campaign called Balloon Array for RBSP Relativistic Losses (BARREL) launched in December 2008 and measured x-rays up to 10 MeV. The BARREL test flight utilized the same x-ray detector as was onboard MINIS, meaning the dataset has both the high time and the high spectral resolution necessary for analysis of x-rays in the higher MeV range. The focus of this thesis is on the analyzing the bremsstrahlung spectral and temporal characteristics (including unknown spectral peaks) of the x-ray spectrum as well as estimating the precipitating electron spectrum, rather than on identifying specific loss

mechanisms. Unlike previous research, energies greater than 1.4 MeV will be characterized.

A case study is presented of the radiation belt precipitation x-ray spectra from one event that took place on February 14th during the BARREL test flight. First, an overview of the new balloon campaign and its x-ray detector will be presented. The techniques developed for correcting and calibrating the dataset using methods from previous balloon x-ray datasets will be described in detail. The observations of the corrected bremsstrahlung spectra and the general picture of magnetospheric activity will be discussed. Three areas of data analysis are covered: analyzing and comparing temporal characterization of the x-ray spectra with previous research; estimating the parent electron spectra and how they compare with available spacecraft observations, and investigating particular spectral characteristics such as unknown peaks. Finally, conclusions from the study are specified and future work is proposed.

Instrumentation

The Balloon Array for RBSP Relativistic Electron Losses (BARREL) campaign is a multi-payload investigation designed to support the Radiation Belt Storm Probe (RBSP) satellite mission. RBSP will launch two spacecraft in 2012 to study the physical dynamics of the radiation belts [*JHU/APL*]. The BARREL mission includes two separate campaigns from Antarctica during the RBSP mission. Each campaign will launch 20 balloons (with balloons launched one to two days apart) to study electron precipitation.

The first Antarctic test flight for BARREL was launched on December 28, 2008. The chief components (i.e., x-ray detector, solar panels, magnetometer) of the BARREL design were flown by "piggybacking" onto another balloon payload; thus, the flight is termed the Piggyback flight. The payload was attached to an ultra-long-duration type of super pressure balloon, which allowed for an extremely long flight of 54 days. **Figure 3** is an overlay of the balloon's trajectory on the Antarctic continent, with each color representing a different day. The balloon was at an average altitude of 34 kilometers while it circumnavigated the South Pole several times before being terminated on February 19th.

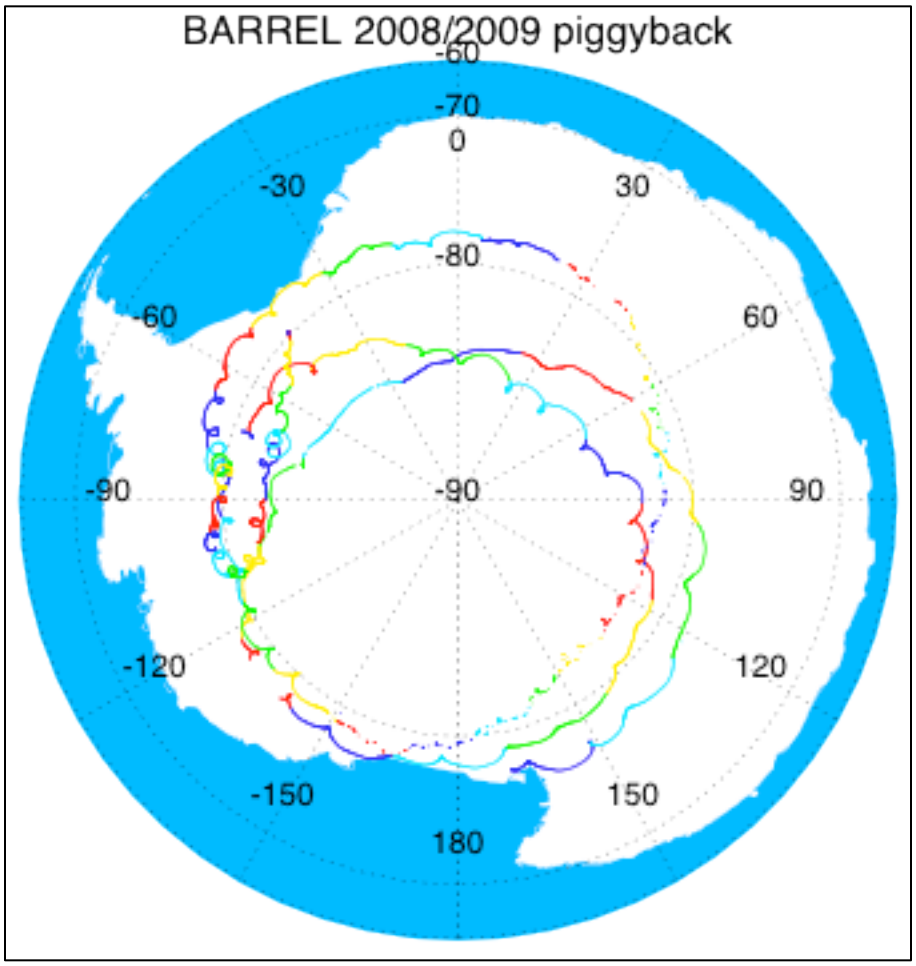

Figure 3. The trajectory of the BARREL Piggyback test flight from December 2008 to February 2009. The coordinates listed are geographic latitude and longitude.

The x-ray detector onboard the BARREL Piggyback flight was the same detector used during the MINIS campaign, consisting of a single 3" x 3" NaI scintillator detector coupled with a photomultiplier tube (PMT). These components, together with a high voltage converter and a preamplifier, are housed inside an aluminum tube, as seen in **Figure 4**. The aluminum tube is placed inside the pink Styrofoam when it is inside the BARREL payload in an effort to mitigate temperature

fluctuations. The electronic boards in **Figure 4** attached to the aluminum tube are the data processing unit (DPU), which converts the detector signal into data output.

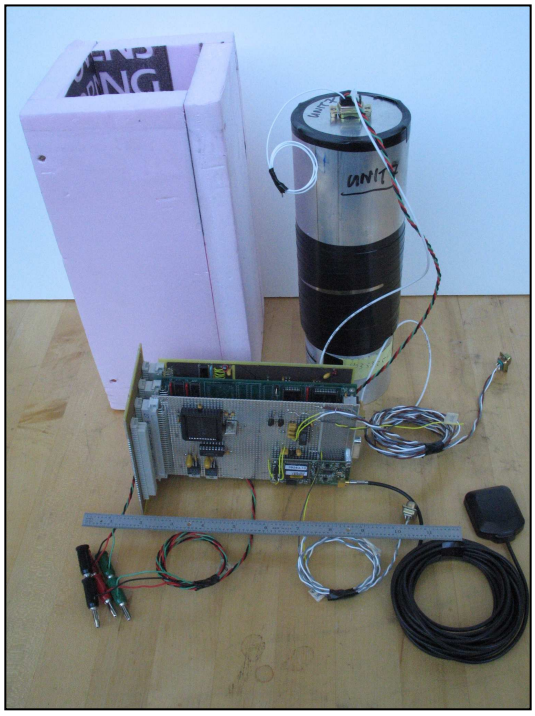

Figure 4. A photograph of the x-ray detector components: the aluminum tube (with a PMT, scintillator, high-voltage converter, and preamp inside), Styrofoam casing, and signal-processing electronics.

The detector measures the energy of an x-ray through a simple process. An x-ray photon hits the scintillator inside the tube and the interaction between the scintillator material and the x-ray photon creates visible light, which travels into the PMT. The PMT converts the light pulse into charge pulse, which is amplified by the pre-amp before being sent to the signal-processing electronics. The DPU receives the charge pulse and converts it into a digital word, which is linearly related to the original x-ray energy (for further information, see *Knoll* [1979]). However one

caveat is that not all x-rays deposit all their energy when interacting with the scintillator. Some x-rays can scatter out of the detector and the true energy of the photon is not recorded. Another caveat is that cosmic rays can also deposit energy as they pass through the detector. Therefore there is certain level of uncertainty involved with the collected data.

The x-ray data is collected into 4096 bins, each nominally 2.4 keV wide, but re-binned and stored in three different modes: the fast, medium, and slow spectra modes. The fast spectra data consist of only four bins (10 – 180 keV, 180 – 550 keV, 550 – 840 keV, and 840 keV – 1.5 MeV) and does not contain the full energy range of the detector, but the data are collected at a very high resolution of 50 msec. The slow spectra mode data contains the full energy range of the detector of 0 – 10 MeV, distributed over 256 bins, with each spectrum collected over 32 seconds. The first 64 bins are nominally 2.4 keV wide, such that the first bin collects counts that occur in the energy range of 0 to 2.4 keV, the next bin collects counts with energies 2.4 to 4.8 keV, and so forth. In higher energy ranges, the bin widths get progressively larger to account for the decrease in counts as the energy increases, thus avoiding large numbers of bins with zero counts. **Table 1** is a display of all the bin widths and their corresponding bin numbers for the slow spectra mode.

Table 1. The bin width (keV/bin) of each new bin after re-binning 4096 bins into 256 bins for the slow spectra mode.

Bin Number	Bin Width (keV/bin)
1 – 64	2.4
65 – 96	4.8
97 – 128	9.6
129 – 160	19.2
161 – 192	38.4
193 – 224	76.8
225 – 256	153.6

The medium spectra mode compresses the slow spectra mode bins into 48 bins by using the equation: mediumbin = floor[9 * (slowbin – 42)], where slowbin is the slow spectra mode bins 42 through 212. The medium spectra mode collects data every 4 seconds and covers energies between 100 and 4000 keV. Even though the detector measures energies less than 10 keV and greater than 8000 keV, the data in those ranges are unreliable because they are close to the detector limits and will not be considered in this study. These data, along with other telemetry and magnetometer data are transmitted to a ground station through Iridium satellite modems.

Methodology

In order to analyze spectral peaks and temporally characterize the x-ray spectra, the raw data had to be corrected for known instrument behavior. Previous balloon research [*Foat et al.*, 1998; *Millan et al.*, 2002] presented calibrated and background-subtracted data for analysis. In order to compare results from other balloon studies, the same methods were applied, though specially adapted for the particular needs of this dataset, which will be explained further along.

Before beginning with calibration, intervals of interest were selected from the Piggyback flight. The fast spectra data were used as a means to get a short summary of daily activity. **Figure 5** is an example of fast spectra data plotted as a count rate time series during one full day.

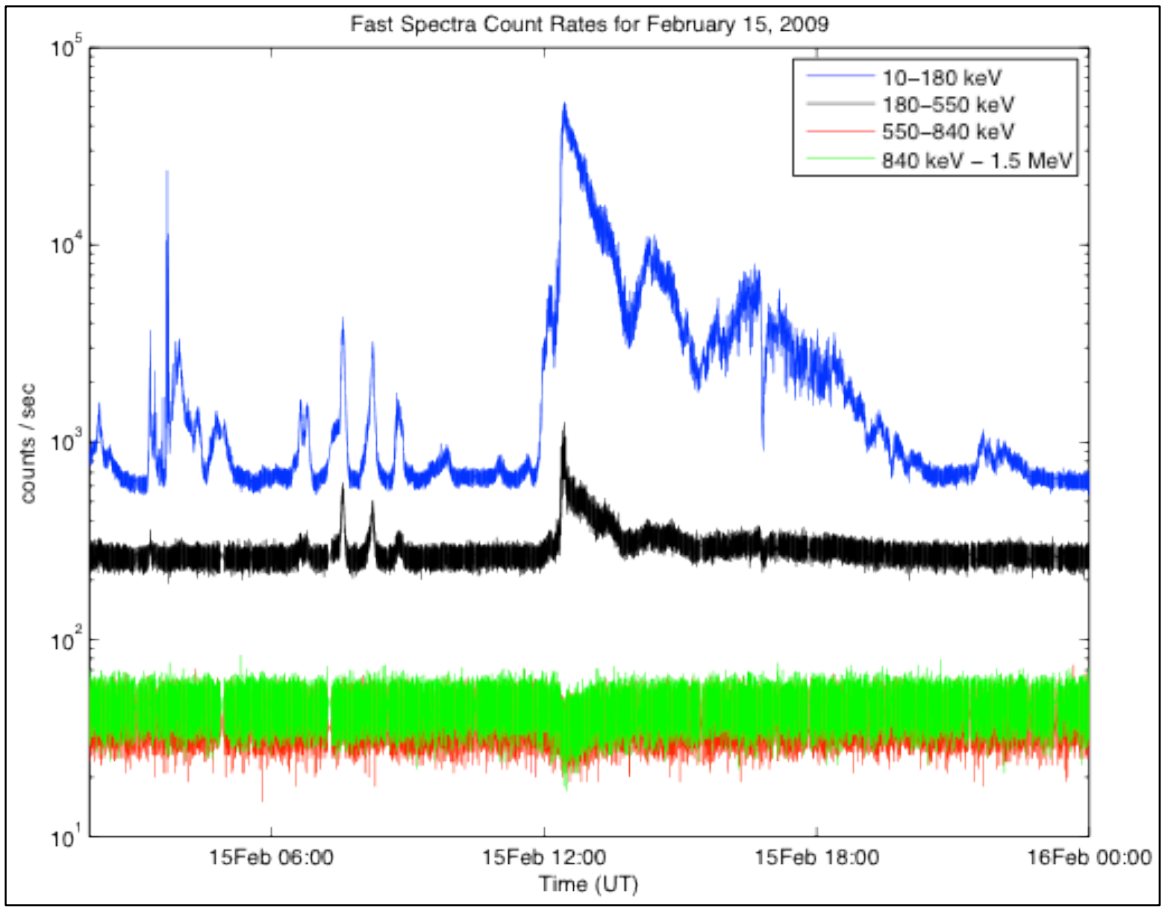

Figure 5. An example of the fast spectra measurements during the Piggyback flight. This day, Feb. 15th, showed increased count rates in all channels around 12 UT.

Figure 5 shows a large amount of activity in the first two channels (blue and black lines), and a small amount of activity in the latter two channels (red and green lines), particularly beginning around 12:00 UT through 20:00 UT. An "event" was selected as an interval of interest when there was an order of magnitude or greater increase in more than one channel for at least several hours. In this "event" on Feb. 15th from around 12:00 to 20:00 UT, the first two channels had a sudden onset of increased count rates that slowly decreased over several hours. Fast spectra were

plotted for other days from the Piggyback flight and events were selected based on the criteria mentioned.

Figure 5 shows there is small drop in count rate in the third and fourth channels with the sudden onset of increased count rate in the first two channels at 12:00 UT. This measurement is an artifact of instrument behavior having to do with dead time. As in most detector systems, there is a certain amount of time after the detector takes to process a measurement before it can take another one. This minimum amount of time the detector needs to separate two events is called dead time. The data must be corrected for the counts that were lost because the detector could not measure them during dead time.

As outlined in *Knoll* [1979], there is a true count rate, n, which the detector would have measured if not for dead time, and a measured count rate, m, which is what the detector actually recorded. The true count rate can be calculated from $n = \frac{m}{1 - m\Delta t}$ where Δt is the dead time per event for the detector. In the case of the Piggyback flight x-ray detector, the dead time per event was about 8 microseconds. The dead time is very small compared to the ten-minute data collection duration, but dead time can become important when the detector is measuring tens of thousands of counts per second. If the difference between the true and the measured counts is greater than the counting statistics ($(n - m)T > \sqrt{N}$), where N is the standard deviation of a Poisson measurement and T is data collection duration, then a dead-time-correction needs to be applied.

Ten-minute-averaged x-ray spectra were created from the slow spectrum data for the events selected and the dead time correction was applied. The data were collected over ten minutes to improve statistics for analysis of spectral peaks and estimates of parent electron populations at higher energies. **Figure 6** is an example of a ten-minute-averaged x-ray spectrum with axes of counts/second/keV versus energy (in units of keV) on February 15, 2009. Referring back to **Figure 5**, this spectrum is observed right before the sudden onset of increased counts at 12:00 UT. The noticeable peak occurring around 511 keV is a well-known line produced by electron-positron annihilation. The fixed energy of the location of this line was used to construct an energy correction to the x-ray spectra.

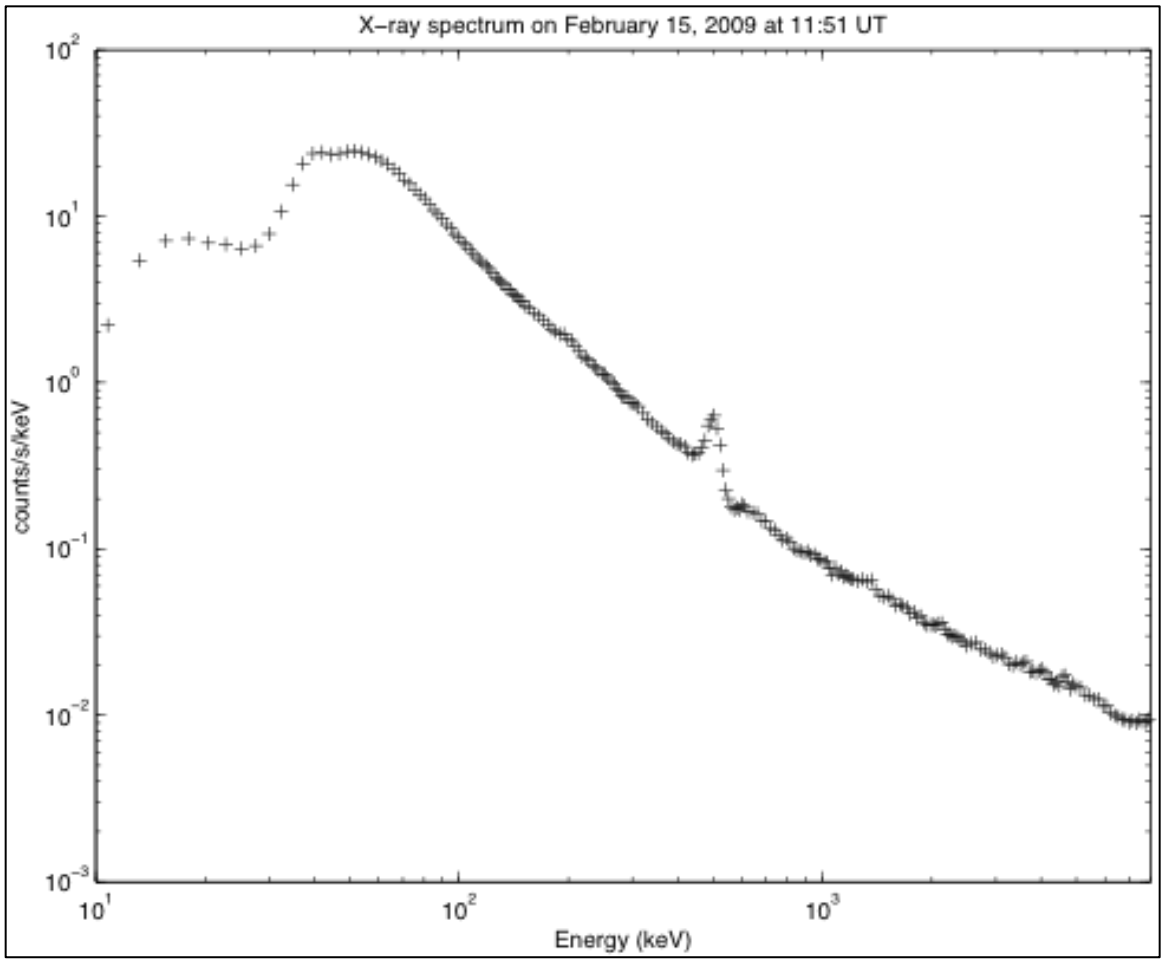

Figure 6. An example of an x-ray spectrum during quiet periods of activity after dead time corrections and re-binning has been performed. The large peak around 511 keV is the electron-positron annihilation line.

As the scintillator in the x-ray detector experienced a range of temperatures (~ 15 degree daily change) during the length of a balloon flight, the relationship between bin number and energy (i.e., the bin widths) changed. This relationship is called the gain. Gain variations resulting from changes in scintillator temperature are a well-known phenomenon, and calibrations using the electron-positron annihilation line have been done for previous balloon flights to correct for these

variations. The annihilation line is known to occur at 511 keV; therefore, the peak of this observed line in each spectrum should occur at 511 keV. The peak location will move as the temperature changes because the gain has changed. Usually, a linear equation can be applied to bin number location of the peak as a function of temperature for correcting the gain variation.

However, in this dataset that equation could not be applied (see Appendix A). Instead, an assumption was made that the variation in the bin location of the 511 keV peak must be due to gain changes, so each spectrum's gain was individually scaled such that the peak in counts due to the annihilation line resided in the energy bin that contained 511 keV. This method calculated the actual gain each spectrum instead of the previously assumed 2.4 keV/bin gain. However, in order to compare spectra, the data were interpolated and re-binned to the original gain of 2.4 keV/bin. Using this method, every spectrum was uniformly calibrated.

The next step was to subtract out the background x-ray spectrum. Looking back at **Figure 5**, it is apparent that there is some constant x-ray background activity in each channel because the count rate drops to the same level after some kind of event occurs. For example, the first channel always returns to about 700 counts s^{-1} and the second channel always returns to about 300 counts s^{-1} during the time span of the plot. This x-ray background was created by some known (cosmic rays, radioactive decay) and unknown sources that vary slowly over the duration of the balloon flight. Some background x-rays may even be produced by electron precipitation from the magnetosphere [*Kennel and Petscheck*, 1966]. However, the focus of this research is on the large increases and minute to hourly changes in the

x-ray spectrum, therefore the background should be subtracted off in order to examine just x-rays pertinent to this study.

However, the x-ray background is not constant throughout the duration of the Piggyback flight because the balloon travels through different regions of the magnetic field and observes different x-ray sources. Therefore, spectra from very quiet hours-long periods before each event were averaged to create a background spectrum. **Figure 7** is an example of a background spectrum, which was used for events on February 14th and 15th.

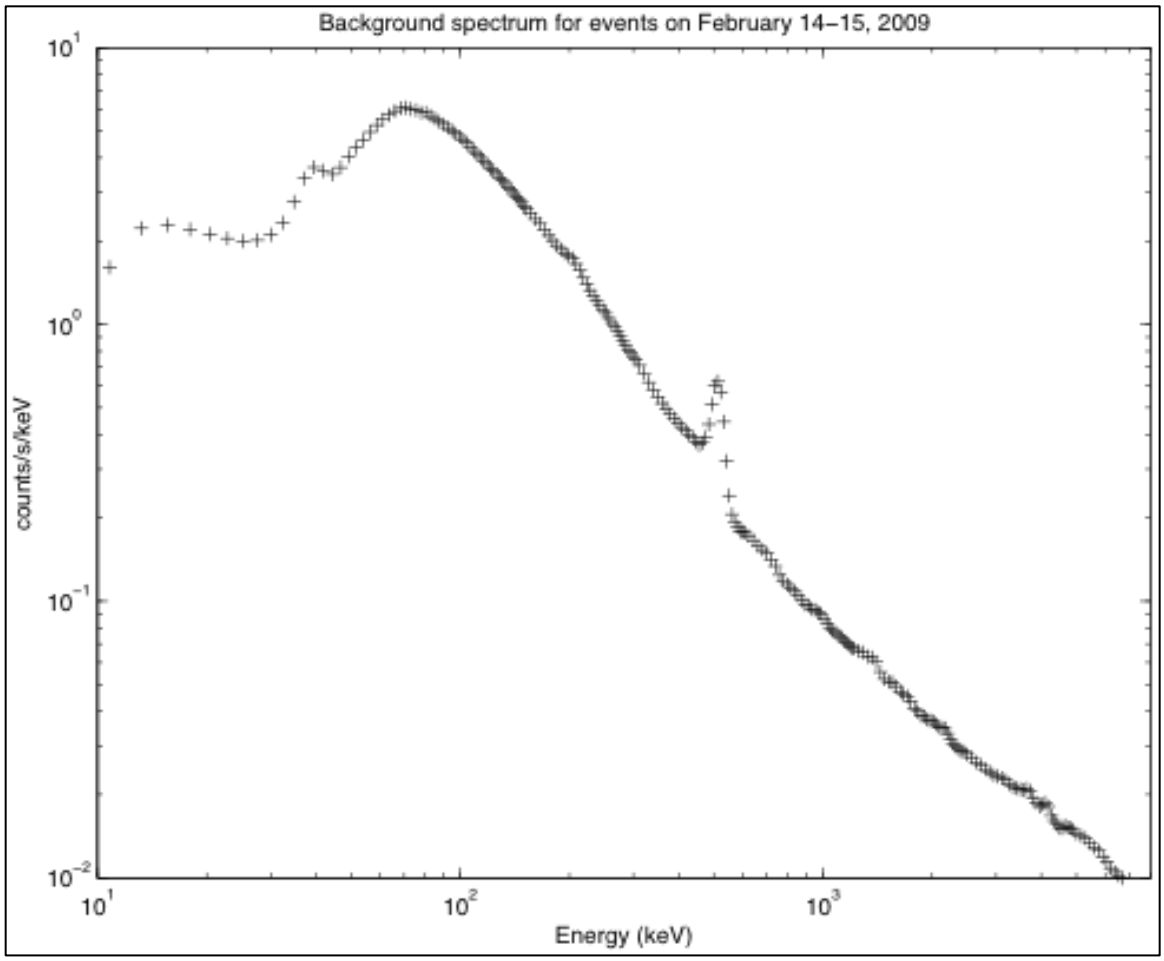

Figure 7. An averaged spectrum from February 12, 2009 4 – 9 UT, which is used as a background spectrum for the events on February 14th – 15th.

This background spectrum is an average of all spectra on February 12, 2009 from 4 – 9 UT. The error bars were not plotted because the calculated errors were between .04% and 5% of the measured count rates, which were too small to be seen in the figure. The change in count rate in each channel in the fast spectra over this duration was less than the standard deviation of count rate. This was the criterion applied when selecting background intervals.

The residual data represents the x-ray spectra measured inside the detector, but not the spectra of the original bremsstrahlung x-rays. As bremsstrahlung x-rays travel through the atmosphere, some photons are lost to Compton scattering and absorption. The aluminum shield around the detector also absorbs some amount of photons. In order to analyze the spectra of the original x-ray bremsstrahlung created from the precipitating electrons at the top of the atmosphere, the losses from the atmosphere and the detector must be added back. *Holt* [1970] states that the fraction of photons removed while passing through a medium is $\frac{dI}{I} = -\mu\, dx$, where μ is mass attenuation coefficient (with units of $cm^2\ g^{-1}$). For a finite thickness x, this equation can be integrated to $I = I_0 e^{-\mu x}$ where I_0 is the original count rate of photons. The thickness (x) in the previous equation, which has units of $g\ cm^{-2}$, is called an interaction depth and describes the amount of material that the photon passes through. This above equation can be applied to losses from both air and aluminum.

Beginning with aluminum, the density (ρ) is assumed to be a constant 2.7 $g\ cm^{-3}$ and the aluminum casing is about .1 cm thick (l). Calculating the interaction depth needed for the above equation is straightforward in this instance: $x = \frac{\rho}{l}$. The interaction depth for aluminum is .27 $g\ cm^{-2}$. **Figure 8** is a sample of the mass attenuation and mass energy absorption coefficients for aluminum as a function of energy. The data provided in **Figure 8** was interpolated for the desired energies and applied to the equation from *Holt*.

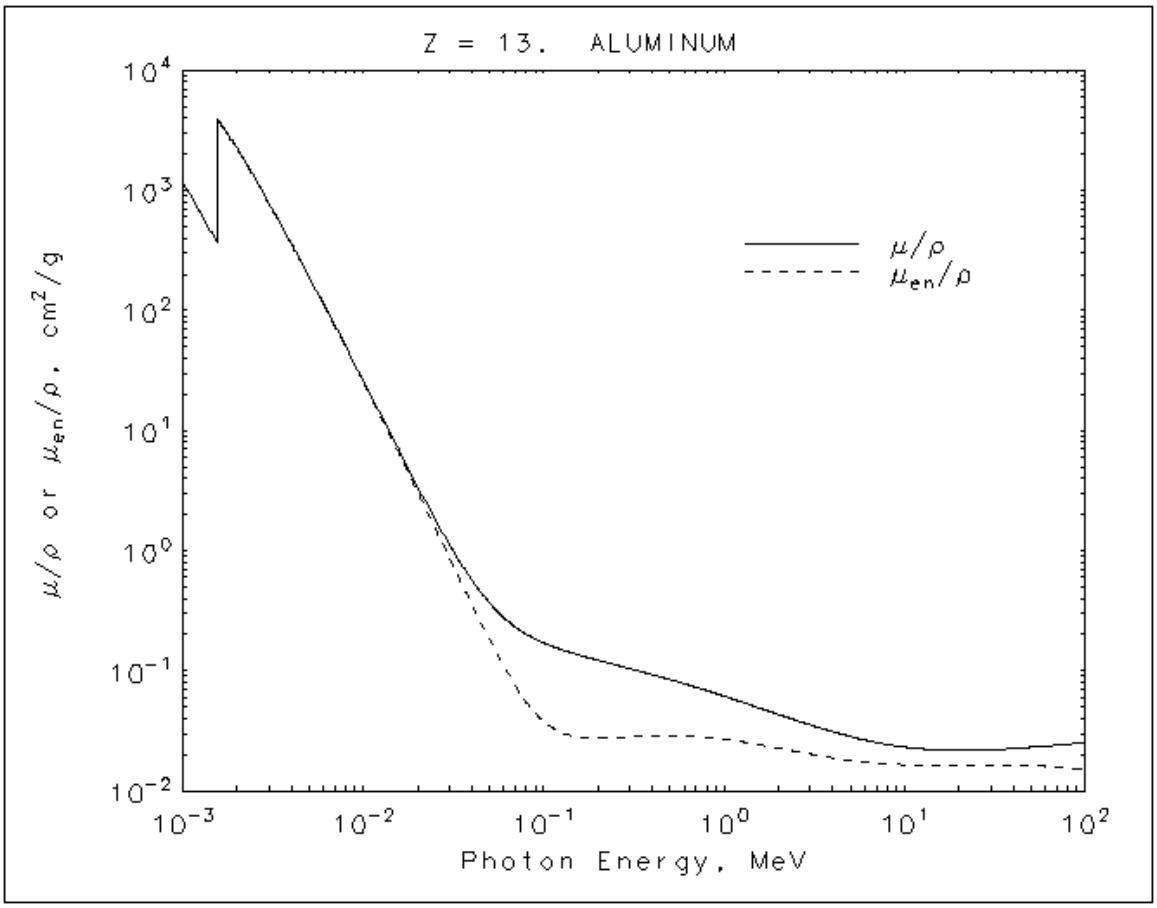

Figure 8. The mass attenuation (solid line) and mass energy absorption (dashed line) coefficients for aluminum as a function of photon energy [*Image provided by the IRCU,* 1980].

Unfolding the losses from air was also straightforward by using calculated values from the *Handbook of Physics and Chemistry* [2009-2010]. The interaction depth was calculated using $x = \frac{P}{g}$, where the pressure (P) at 35 km is listed as 574.6 kg m^{-1} s^{-2}, and gravity (g) at 35 km is 9.7 m s^{-2}, which gives an interaction depth of 59.23 km m^{-2} or 5.9 g cm^{-2}. **Figure 9** is the mass attenuation and mass energy absorption coefficients for air. These mass attenuation coefficients were also interpolated and also used in the *Holt* equation.

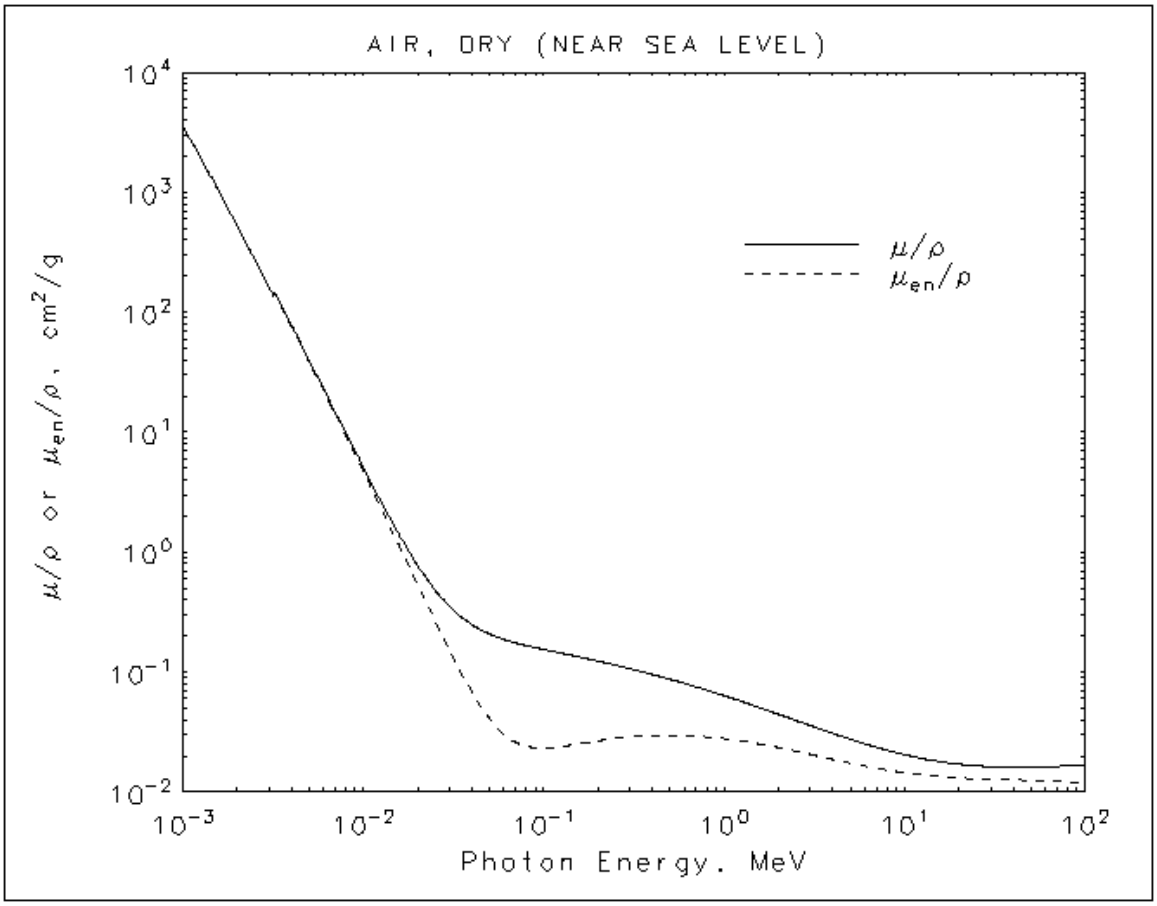

Figure 9. The mass attenuation (solid line) and mass energy absorption (dashed line) coefficients for air as measured near sea level as a function of photon energy [*Provided by the IRCU,* 1980].

Figure 8 and **Figure 9** illustrate that more photons are lost at lower energies, and therefore the difference between the x-ray spectra measured by the detector as compared with the spectra measured at the top of the atmosphere should be greater at lower energies. The new x-ray spectra calculated with the method outlined above demonstrate this relationship; one example spectrum is shown in **Figure 10**. Error bars for each point in the figure were calculated by

applying error propagation techniques to the original uncertainties associated with each energy bin.

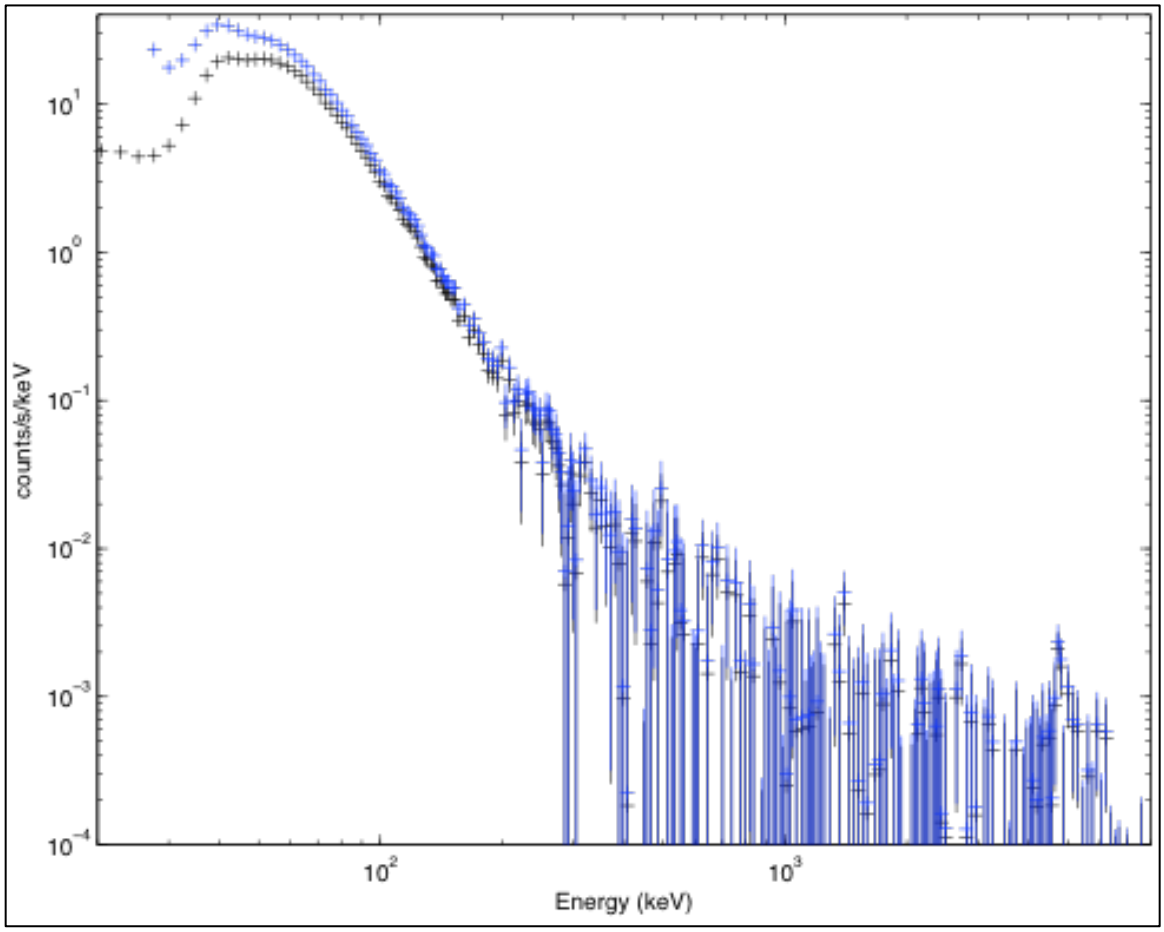

Figure 10. The x-ray spectrum plotted as measured inside the detector (black line) and the spectrum at the top of the atmosphere (blue line) from Feb. 15, 2009 at 11:51 UT. Error bars have been plotted for some points from each spectrum.

Finally, the data were converted into units of flux (counts s^{-1} keV^{-1} cm^{-2}) by dividing by the detector area of 58 cm^2. Analysis was performed on photon energies between 90 and 8000 keV. This method was applied to each ten-minute-averaged spectrum from the intervals selected for events.

Observations

During the 54-day Piggyback flight, only six events met the criteria discussed in the previous section because geomagnetic activity was rather quiet. **Figure 11** displays the Dst index time series during the bulk of the Piggyback flight. Dst is a geomagnetic index that is derived from an hourly average of the horizontal component perturbations of the Earth's magnetic field from four low-latitude observatories. During storm times, a large-scale current system around the Earth called the ring current grows, thus reducing the horizontal component of the terrestrial magnetic field. Therefore, the larger the storm, the more negative the Dst index will become [*Baumjohann and Treumann*, 1996]. Typical geomagnetic storms, such as the solar flare during MINIS, have a peak Dst of -100 nanoTesla (nT), while larger storms such as the Bastille Day storm of July 2000 reached a peak Dst of -300 nT [*WDC for Geomagnetism*, 2010]. As **Figure 11** shows, the activity observed during the Piggyback flight would be considered small.

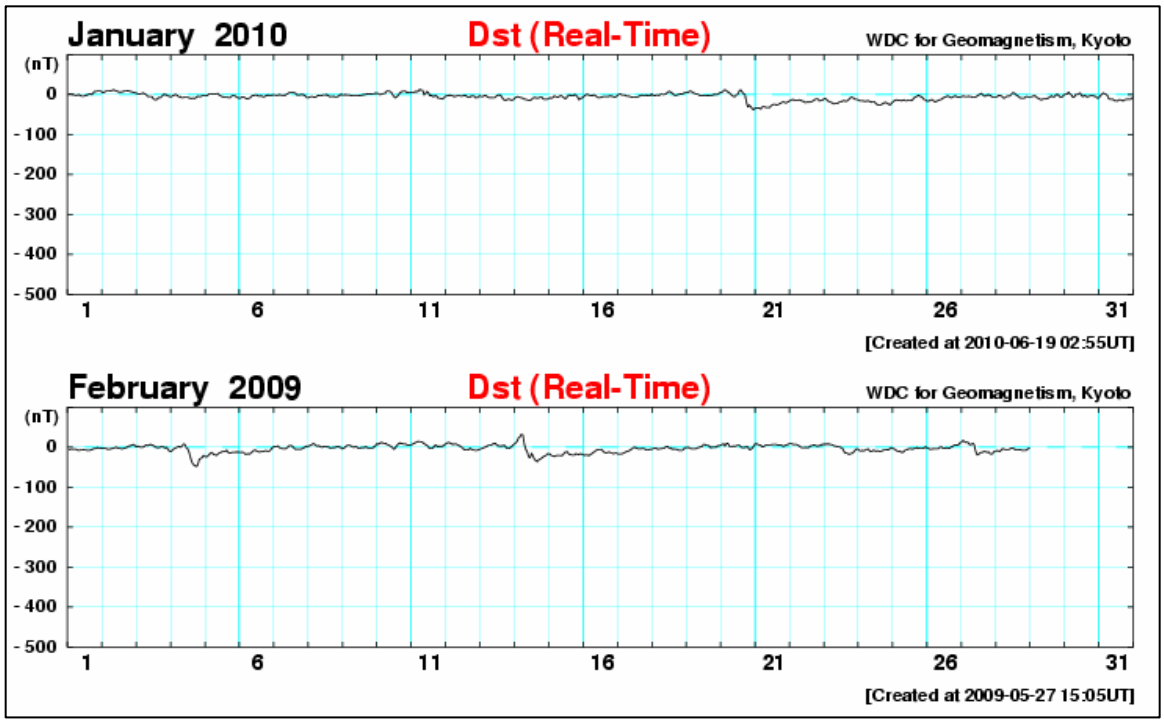

Figure 11. The hourly Dst index (measured in nanoTesla) during January and February 2009 [*Provided by the World Data Center for Geomagnetism, Kyoto,* 2010].

Even though corrections and calibrations were performed for several events during the Piggyback flight, the rest of the thesis is devoted to only one event in an effort to present a thorough and comprehensive analysis that can be applied to more events from this test campaign and to future BARREL data.

The event being analyzed occurred on February 14, 2009 from 12:03 – 17:44 Universal Time (UT). Looking at **Figure 11**, large substorm activity occurred around 12:30 UT on February 14th as indicated by the sudden decrease in Dst. The substorm activity is confirmed by looking at another geomagnetic index called the auroral lower envelope (AL). The AL index is a measure of the westward-moving current in the auroral zone of the ionosphere. At substorm onset, the westward

current increases dramatically as the sudden reconnection in the magnetospheric tail forces all the stored magnetic flux to the dayside and strengthens the westward current in the ionosphere. [*Baumjohann and Treumann*, 1996].

The AL index for February 14, 2009 is plotted in **Figure 12** along with the auroral upper envelope (AU) index, which is a measure of the eastward-moving auroral current. The auroral currents are measured in nanoTesla because the currents are inferred from the northward and southward disturbances in the magnetic field, which are thought to represent changes in the eastward and westward currents respectively. The color of the data shown corresponds to the number of auroral-zone stations that measured the disturbance [*Baumjohann and Treumann*]. **Figure 12** shows a dramatic increase (meaning a more negative value) in AL after 12:00 UT, which is when the event in question began. The AL index shows substorm activity lasted for several hours and the end of the activity was at the end of 18:00 UT.

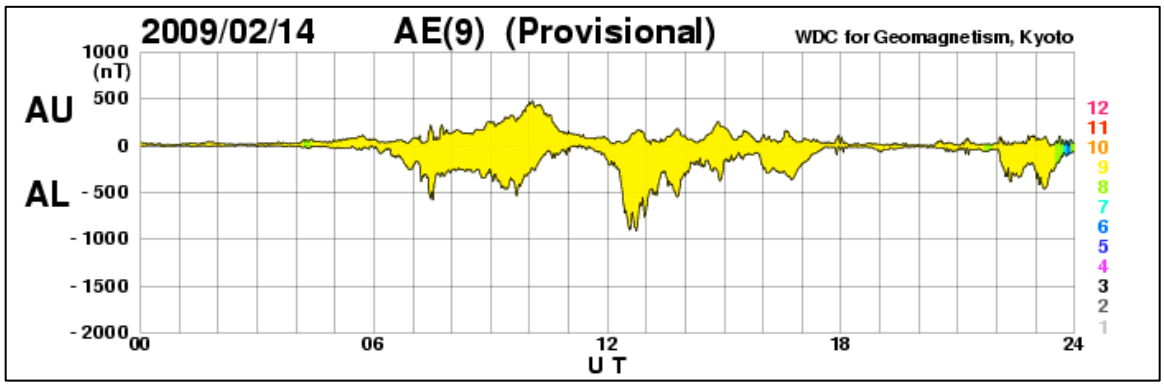

Figure 12. The geomagnetic indices AL and AU as observed on February 14, 2009 [*Data provided by the World Data Center for Geomagnetism, Kyoto*, 2010].

Figure 13 displays the beginning and end of the substorm activity, as reflected in the fast spectra data collected during this time. The vertical lines in the figure mark the times at which AL values (shown in the previous figure) changed significantly. The activity in the lowest-energy channel (blue dots) correlates with the variations seen in AL (though inversely). Both data series experienced a rapid change around 12:30 UT and both returned to quiet levels after 17:30 UT. Furthermore, both data series experience large peaks just before 14:00 UT and 15:00 UT. The other channels did not experience increases as large as the first channel; so higher-spectral resolution data must be analyzed to understand what activity occurred in those energy ranges.

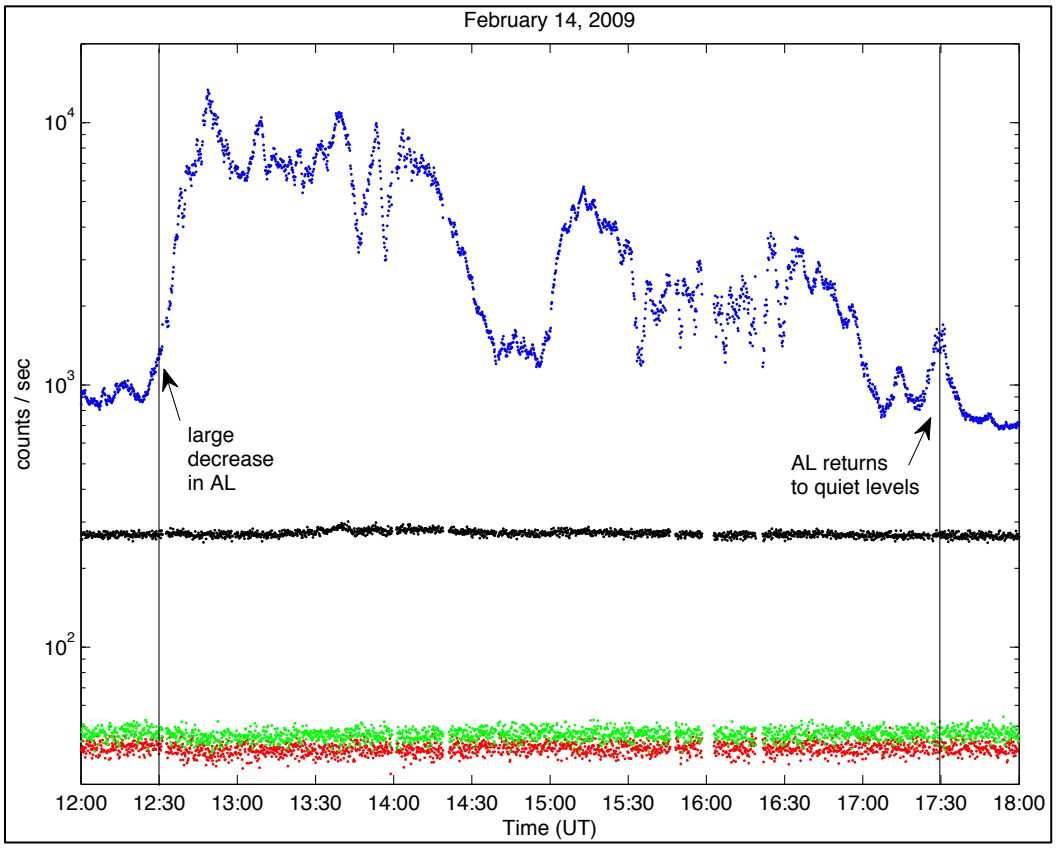

Figure 13. The fast spectra data during the substorm activity. Fast spectra data have four channels: 10 – 180 keV (blue dots), 180 – 550 keV (black dots), 550 – 840 keV (red dots), and 840 keV – 1.5 MeV (green dots).

The solar wind conditions during this time period are summarized in **Figure 14** from the Advanced Composition Explorer (ACE) spacecraft. ACE observed the solar wind approximately 50 minutes before that same solar wind arrived at Earth because ACE was 233 Re in front of Earth in the Earth-Sun line. **Figure 14** shows the solar wind magnetic field vectors as well as flow speed. The red lines on the figure approximately mark the beginning and the end of the solar wind conditions during the event, but propagated to times when ACE was measuring that solar wind. At the beginning of the event, the z-component of the magnetic field (in **Figure 14c**)

turned southward (turned negative), which is a required component of substorm creation. The z-component did not stay negative, but vacillated between positive and negative around 13:00 UT and 14:00 UT. These two peaks correlate with the peaks seen in AL (**Figure 12**) and the fast spectra (**Figure 13**) at about 14:00 UT and 15:00 UT. The solar wind flow speed (**Figure 14d**) averaged around 480 km s^{-1} until it jumped up to 540 km s^{-1} around 15:00 UT.

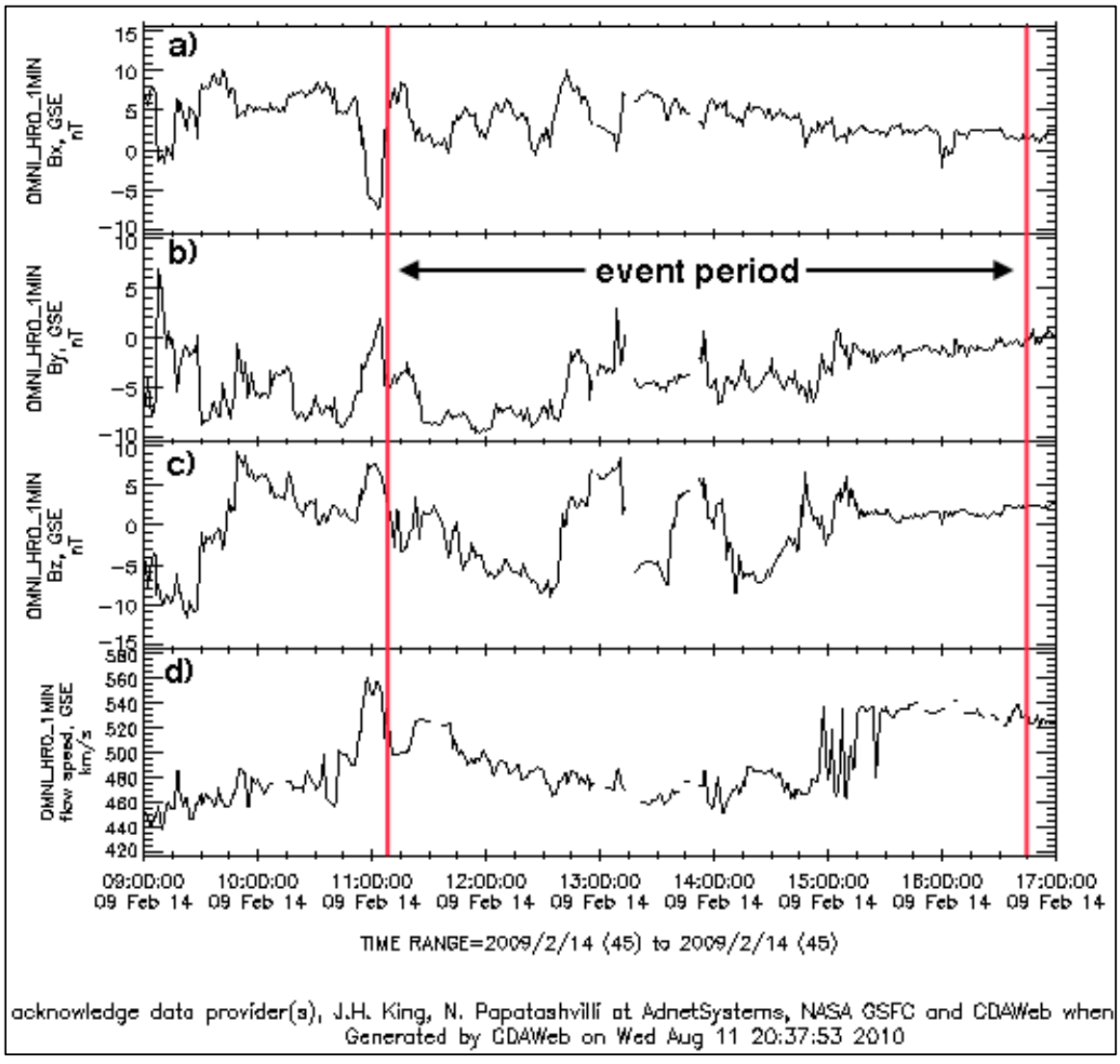

Figure 14. Solar wind magnetic field coordinates and flow speed as measured by ACE.

During this event on February 14th, the balloon carrying the BARREL instruments had an average latitude of 81 degrees south and an average longitude of 105 degrees west. The magnetic local time and L-shell values for each constructed x-ray spectrum were calculated and are plotted in **Figure 14**. Magnetic local time (MLT) is a measure of longitude with reference to the magnetic dipole axis (which is tilted 11 degrees from the spin axis), and is recorded in units of hours, not degrees. In other words, magnetic local time is a reference to a position with respect to the Sun, corresponding to a clock. L-shell value refers to the terrestrial magnetic field line on which a specific location lies on and is measured in Earth radii (Re) from the center of the Earth.

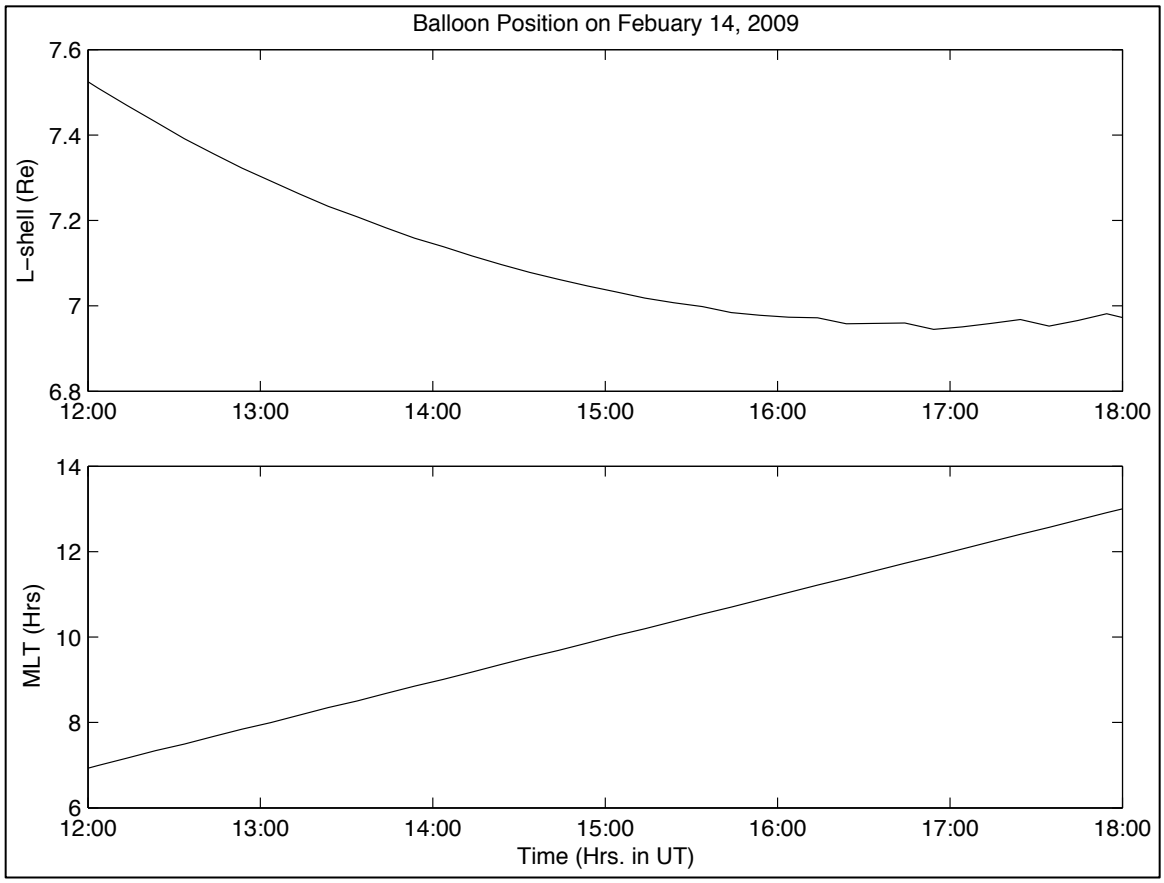

Figure 15. MLT (measured in hours) and L-shell (measured in Earth radii) values of the balloon's location during the event.

MLT and L-shell were calculated from latitude and longitude using the Tsyganenko magnetic field model. The Tsyganenko model is a semi-empirical model of the Earth's magnetic field that outputs position with respect to the magnetic field from latitude, longitude, and time inputs [*Tsyganenko*, 1989]. MLT and L-shell are calculated from the output coordinates with the following equations:

$$L = \sqrt{x^2 + y^2 + z^2}$$
$$MLT = (12/\pi)\left[(\tan^{-1}(y/x) + \pi) \bmod 2\pi\right]$$

The variables x, y, and z are the output coordinates in the Geocentric Solar Magnetospheric (GSM) coordinate system. In the three-dimensional GSM coordinate space, the x-axis points toward the sun, while the y-axis is perpendicular to the Earth's magnetic dipole and the x-z plane contains the dipole axis [*Kivelson and Russell*, 1995].

Figure 15 shows that the balloon was in the morning sector around 0700 when the event began and passed over 1200 into the afternoon sector as the event was ending. The balloon's high latitude (close to the polar cap) means the balloon was mapping out to high L-shells of around 7 Re. As stated before, the outer radiation belt typically exists between 2 and 6 Re, but can extend to higher L-shells during geomagnetic activity. Therefore, satellite data was used to confirm whether the balloon was mapping to the outer radiation belt as opposed to other regions of the magnetosphere. Each of the five satellites in the THEMIS (The Time History of Events and Macroscale Interactions during Substorms) platform has a Solid State Telescope (SST) that measures (among other things) electron distributions of energies in the range of 25 keV to 6 MeV. These energies correspond with outer radiation belt electron energies [THEMIS website, 2010]. Balloon and THEMIS data can be correlated because three of the THEMIS spacecraft were at the same L-shells as the balloon during this event. The SST measurements from one of these spacecraft, THEMIS A, are plotted in **Figure 16**.

The spacecraft measures large increases in electron flux at all energies in the detection range when it passes through the radiation belt. As can be seen in the figure, data were not available for electron energies greater than 2 MeV during this time. THEMIS A experiences the described large increase in flux starting just before 17:00 UT, meaning it passed through the outer radiation belt. The THEMIS spacecraft also observed the radiation belt at the same area the data before as well. The THEMIS data shows that the radiation belt was at distances of about 7 Re, assuming it was at that distance during the whole event, therefore the balloon was measuring radiation belt precipitation.

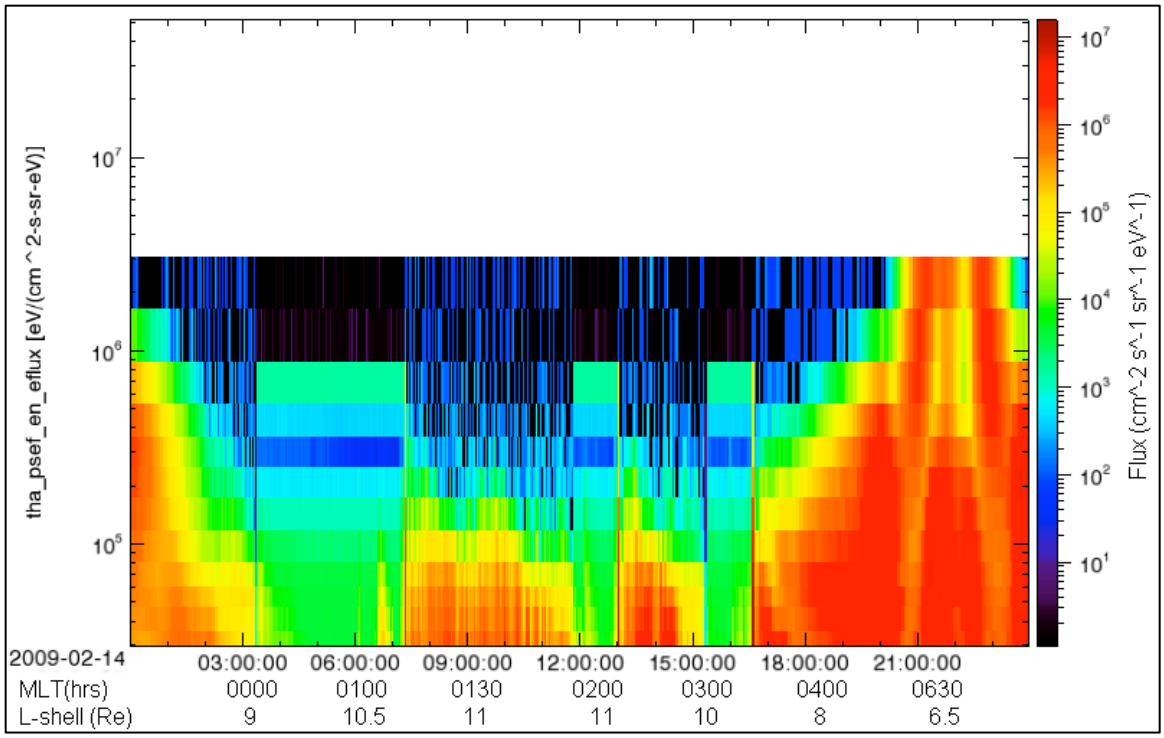

Figure 16. THEMIS A SST spectrogram of electron energy flux spectral plot in time versus energy versus flux, where electron energy is in units of eV, and flux is in units of eV cm^{-2} s^{-1} sr^{-1} eV^{-1}.

From the chosen event on February 14th, 35 spectra were produced for every ten-minute interval. Not all spectra can be presented individually here, but an example spectrum is given in **Figure 17**. The crosses represent the average flux observed in each energy bin while the length of the vertical lines is the magnitude of one standard deviation of that flux in each direction. Point that fell below background levels (negative points) were not plotted, but if the standard deviation line reached above zero, the error bar was plotted. This spectrum occurred at 12:43 UT and is an example of the highest average fluxes measured during the event.

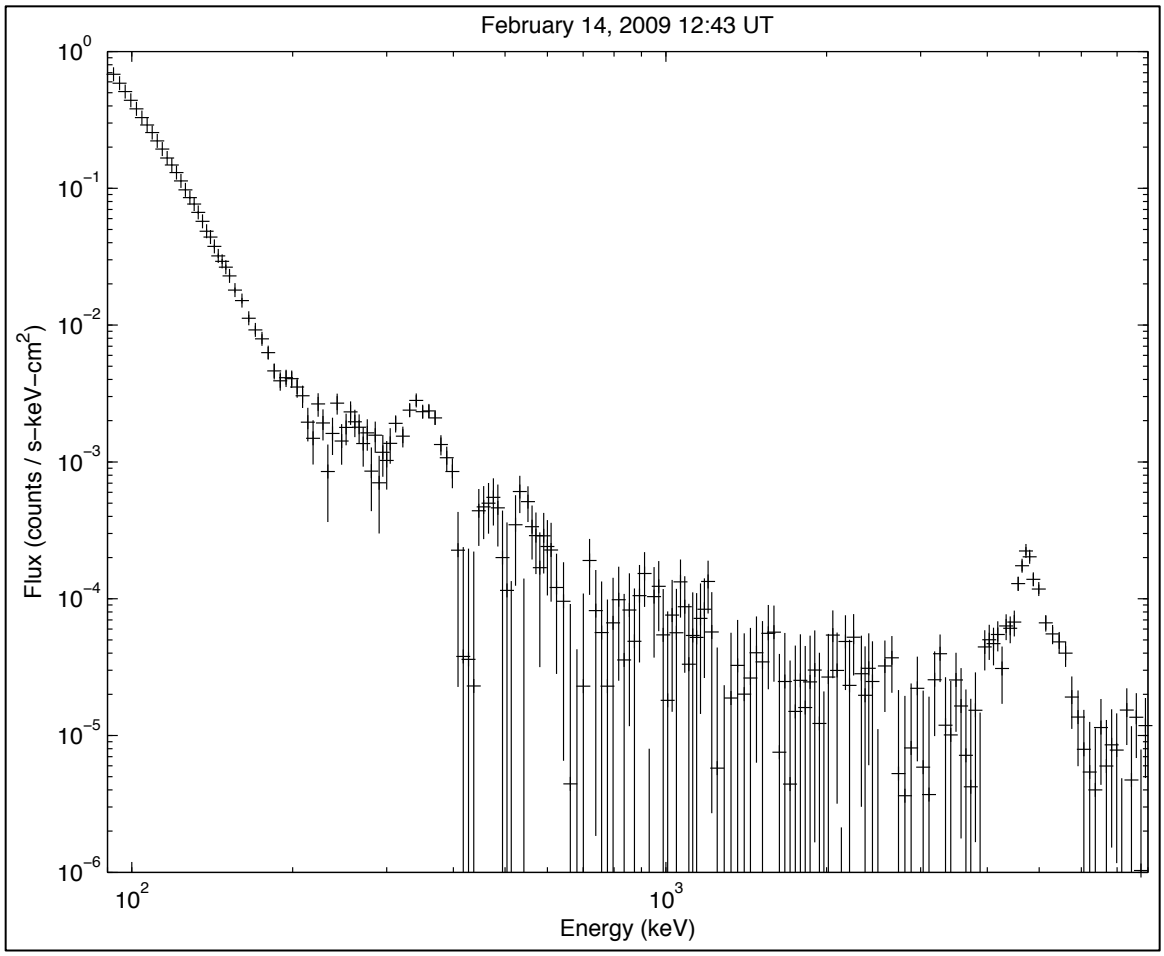

Figure 17. An example spectrum of the flux measured during the event at 12:43 UT. The flux measured in each bin is plotted as a cross with the length of the vertical line corresponding to the magnitude of one standard deviation.

Figure 17 reveals some interesting features observed throughout the Piggyback data. Two prominent spectral peaks that have not been observed by these authors before occur at about 350 keV and 4.8 MeV. The error associated with each point on the spectral peaks is small enough that the two peaks cannot be attributed to noise. The general summary of the behavior of the spectral peaks and the changes in the flux can be seen in **Figure 18**.

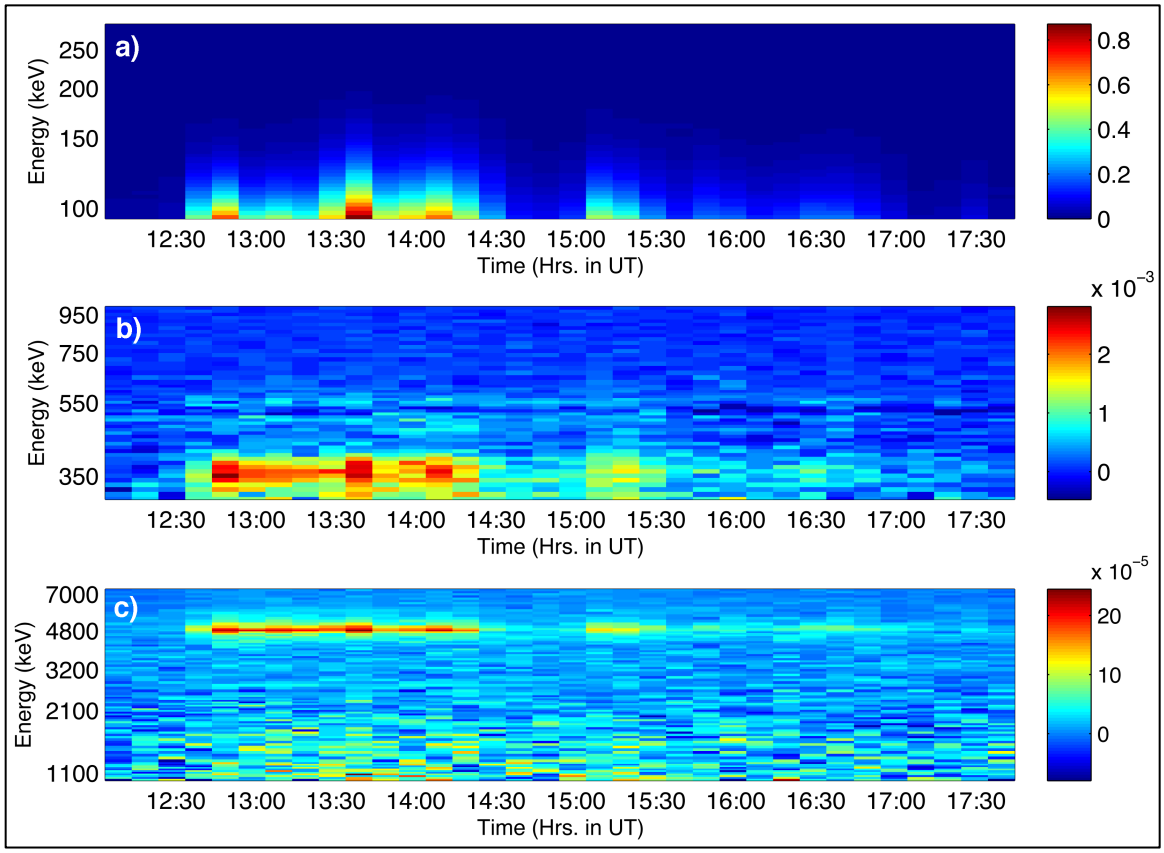

Figure 18. Three spectrograms depicting the general change in flux over all energies during the event, with flux in units of counts s^{-1} keV^{-1} cm^{-2}. (a) covers electron energies 90 – 300 keV, (b) covers electron energies 300 – 1000 keV, and (c) covers electron energies 1000 – 8000 keV.

Three spectrograms are plotted for the following energy ranges from the event spectral data. **Figure 18a**, which covers energies from 90 to 300 keV, summarizes how the largest measured fluxes, which were in the lower energies, generally changed over the course of the event. Increases in flux began around 12:30 UT and reached peak values just after 13:30 UT before falling off at 14:30 UT (with a slight resurgence at 15:00 UT). The measured flux also falls off quickly in

energy, with the highest measured fluxes concentrated around 100 keV. **Figure18b**, which covers energies 300 to 1000 keV, and **Figure 18c**, which covers energies 1 to 8 MeV, illustrate the general behavior of the 350 keV and 4.8 MeV spectral peaks respectively. Their temporal behavior of the spectral peaks seems to correlate with the temporal behavior illustrated in **Figure 18a**.

While these spectrograms provide a good general picture of the temporal behavior of the x-ray spectra, a more quantitative approach is needed to fully characterize the radiation belt losses. The following sections will present a more thorough analysis of the x-ray spectra temporal characteristics and discuss the possible source of the observed spectral peaks.

Characterization of X-ray Spectra

Referring back to **Figure 17**, the x-ray flux as a function of energy follows some general trends such that it could be characterized by some functions. As stated in the introduction, previous research [*Barcus and Rosenberg*, 1996; *Berger and Seltzer*, 1972; *Parks et al.*, 1979] utilized either an exponential or a power law fit to define a single spectrum. However, *Foat et al.* [1998] used two different power laws to fit their data (one for energies less than 250 keV and one for energies greater than 400 keV) since the energy range was over 1 MeV wide. With the large extent of the data used here (an 8 MeV range), it is likely to assume that this current dataset will also require two different functions at lower and higher energies to characterize the full energy spectrum.

Beginning with the lower energies (90 – 200 keV), an exponential function was chosen to fit the data because the previous work mentioned above accurately described the data this way. To find the best exponential fit, the least-squares method from *Bevington and Robinson* [2003] was applied. The least-squares method seeks the parameters a and b from a linear equation $y(x) = a + bx$ that minimizes the difference between the data and the y-values from the linear equation using a goodness-of-fit parameter χ^2, where $\chi^2 = \sum \left[\frac{y_i - y(x_i)}{\sigma_i} \right]^2$. The measured value is y_i, its uncertainty is σ_i, and the calculated value from the linear function is $y(x_i)$. The goal is to minimize χ^2 in order to find the parameters a and b that constitute the best-fit function.

The least-squares method can be applied to non-linear functions by transforming them into linear functions. An exponential equation of the form $y = Ae^{bx}$ where x is energy and $A = e^{a}$ can be transformed into a linear equation ($\ln y = a + bx$) by taking the natural logarithm of both sides. Now $\chi^2 = \sum\left\{\frac{1}{\sigma_i'^2}\left[\ln y_i - a - bx_i\right]^2\right\}$ where $\sigma_i' = \sigma_i \frac{d(\ln y_i)}{dy} = \frac{\sigma_i}{y_i}$ to account for error propagation. To find the values of a and b that will give the minimum value of χ^2, the partial derivatives of χ^2 with respect to each parameter are set to zero:

$$\frac{\partial \chi}{\partial a} = \sum_{i=1}^{n} -\frac{2y_i^{\,2}}{a\sigma_i^{\,2}}(\ln y_i - a - bx_i) = 0$$

$$\frac{\partial \chi}{\partial b} = \sum_{i=1}^{n} -\frac{2y_i^{\,2}}{\sigma_i^{\,2}} x_i(\ln y_i - a - bx_i) = 0$$

The partial derivatives are summed over n, which is the number of data points the exponential line should fit to. These derivatives can be rearranged into linear simultaneous equations with the form $B\phi + c\theta = D$and $E\phi + F\theta = G$, where $\phi = a$ and $\theta = b$.

$$\sum_{i=1}^{n} \frac{y_i^{\,2}}{\sigma_i^{\,2}} \ln y_i = a\sum_{i=1}^{n} \frac{y_i^{\,2}}{\sigma_i^{\,2}} - b\sum_{i=1}^{n} \frac{y_i^{\,2}}{\sigma_i^{\,2}} x_i$$

$$\sum_{i=1}^{n} \frac{y_i^{\,2}}{\sigma_i^{\,2}} \ln y_i x_i = a\sum_{i=1}^{n} \frac{y_i^{\,2}}{\sigma_i^{\,2}} x_i - b\sum_{i=1}^{n} \frac{y_i^{\,2}}{\sigma_i^{\,2}} x_i^{\,2}$$

Solutions for a and b can be quickly solved with the method of determinants where

$$\phi = \frac{\begin{vmatrix} D & C \\ G & F \end{vmatrix}}{\begin{vmatrix} B & C \\ E & F \end{vmatrix}} \qquad \theta = \frac{\begin{vmatrix} B & D \\ E & G \end{vmatrix}}{\begin{vmatrix} B & C \\ E & F \end{vmatrix}}$$

Inserting the terms from the linear equations into the above formulas yields the solutions for both parameters:

$$a = \frac{\sum_{i=1}^{n} \frac{y_i^2}{\sigma_i^2} \ln y_i \sum_{i=1}^{n} \frac{y_i^2}{\sigma_i^2} x_i^2 - \sum_{i=1}^{n} \frac{y_i^2}{\sigma_i^2} x_i \sum_{i=1}^{n} \frac{y_i^2}{\sigma_i^2} x_i \ln y_i}{\sum_{i=1}^{n} \frac{y_i^2}{\sigma_i^2} \sum_{i=1}^{n} \frac{y_i^2}{\sigma_i^2} x_i^2 - \left(\sum_{i=1}^{n} \frac{y_i^2}{\sigma_i^2} x_i \right)^2}$$

$$b = \frac{\sum_{i=1}^{n} \frac{y_i^2}{\sigma_i^2} \sum_{i=1}^{n} \frac{y_i^2}{\sigma_i^2} x_i \ln y_i - \sum_{i=1}^{n} \frac{y_i^2}{\sigma_i^2} \ln y_i \sum_{i=1}^{n} \frac{y_i^2}{\sigma_i^2} x_i}{\sum_{i=1}^{n} \frac{y_i^2}{\sigma_i^2} \sum_{i=1}^{n} \frac{y_i^2}{\sigma_i^2} x_i^2 - \left(\sum_{i=1}^{n} \frac{y_i^2}{\sigma_i^2} x_i \right)^2}$$

The parameters were calculated and an exponential function ($y = Ae^{bx}$, where $A = e^a$) was constructed for each spectrum from the event where x is the mid-point energy for each spectral bin. **Figure 19** displays three examples of the data (black crosses) and the fitted exponential line (red line). Each subplot is a different ten-minute-averaged spectrum near the beginning of the event when flux began to increase. As the flux increases with each successive spectrum, the fitted exponential function also increases in slope and amplitude to match. Each spectrum during the event has a similarly well-fitted exponential function as these example spectra. **Figure 19** shows that the least-squares method was successful in finding the parameters that gave a best fit for the lower-energy data for each spectrum.

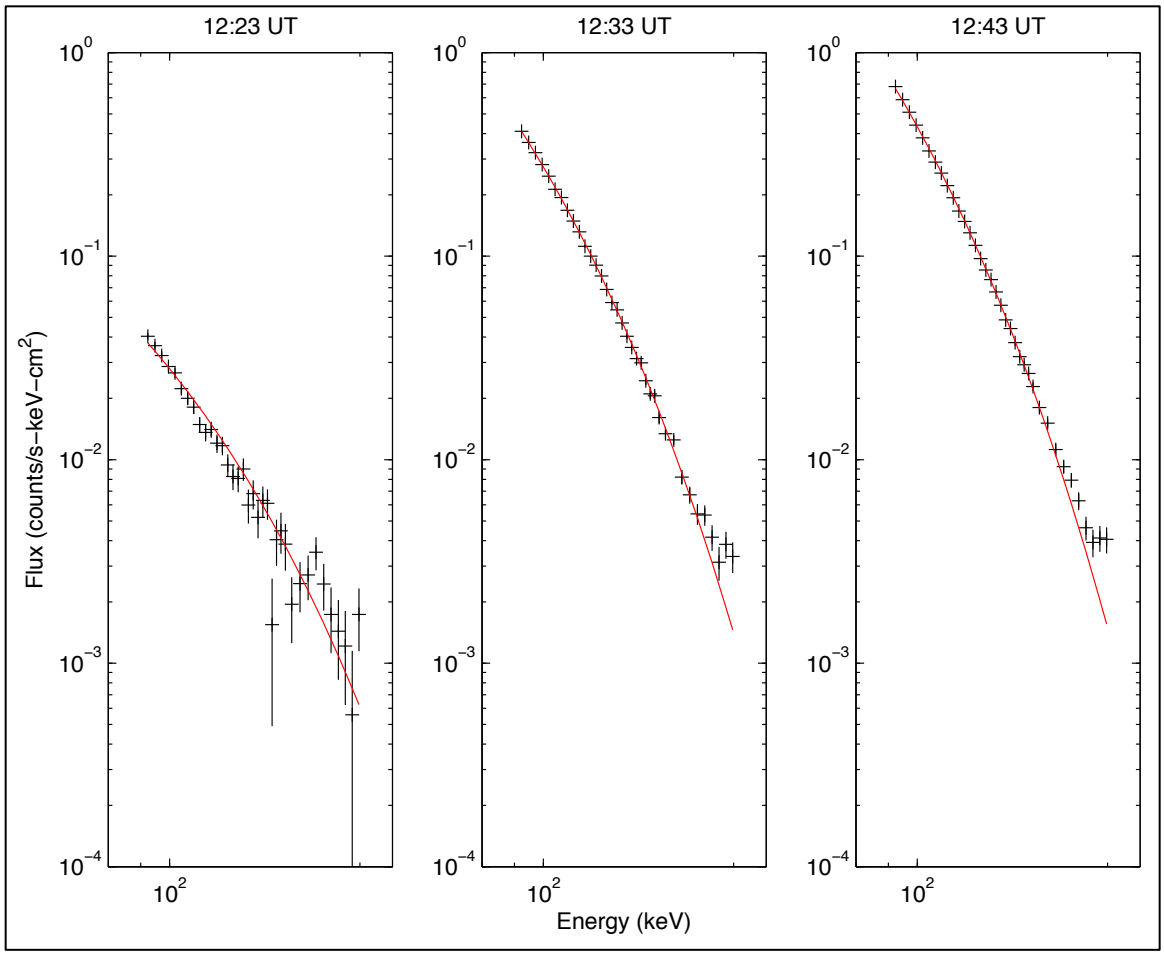

Figure 19. Three spectra of the 90 – 200 keV x-ray data (black crosses) with their corresponding exponential fit (red line).

The error associated with each exponential parameter was also calculated using *Bevington and Robinson*. The general error propagation equation $\sigma_z^2 = \sum \sigma_i^2 \left(\frac{\partial z}{\partial y_i} \right)^2$ was applied to calculate the uncertainties for a and b:

$$\sigma_a^{\,2} = \frac{\sum_{i=1}^{n} \frac{y_i^{\,2}}{\sigma_i^{\,2}} x_i^{\,2}}{\sum_{i=1}^{n} \frac{y_i^{\,2}}{\sigma_i^{\,2}} \sum_{i=1}^{n} \frac{y_i^{\,2}}{\sigma_i^{\,2}} x_i^{\,2} - \left(\sum_{i=1}^{n} \frac{y_i^{\,2}}{\sigma_i^{\,2}} x_i \right)^2}$$

$$\sigma_b^{\,2} = \frac{\sum_{i=1}^{n} \frac{y_i^{\,2}}{\sigma_i^{\,2}}}{\sum_{i=1}^{n} \frac{y_i^{\,2}}{\sigma_i^{\,2}} \sum_{i=1}^{n} \frac{y_i^{\,2}}{\sigma_i^{\,2}} x_i^{\,2} - \left(\sum_{i=1}^{n} \frac{y_i^{\,2}}{\sigma_i^{\,2}} x_i \right)^2}$$

The higher energy (1.4 – 8 MeV) x-ray data appeared to be in straight line on a log-log plot, which is the same attribute of a power law function. Therefore, a power law was fitted to the higher energy data using the same least-squares method summarized above. A power law equation of the form $y = Ax^b$ where $A = e^a$ can be transformed into the linear equation $\ln y = a + b \ln x$. Now

$\chi^2 = \sum \left\{ \frac{y_i^{\,2}}{\sigma_i^{\,2}} \left[\ln y_i - a - b \ln x_i \right]^2 \right\}$ and the linear simultaneous solutions appear as:

$$\sum_{i=1}^{n} \frac{y_i^{\,2}}{\sigma_i^{\,2}} \ln y_i = a \sum_{i=1}^{n} \frac{y_i^{\,2}}{\sigma_i^{\,2}} - b \sum_{i=1}^{n} \frac{y_i^{\,2}}{\sigma_i^{\,2}} \ln x_i$$

$$\sum_{i=1}^{n} \frac{y_i^{\,2}}{\sigma_i^{\,2}} \ln y_i \ln x_i = \sum_{i=1}^{n} \frac{y_i^{\,2}}{\sigma_i^{\,2}} \ln x_i - \sum_{i=1}^{n} \frac{y_i^{\,2}}{\sigma_i^{\,2}} \ln x_i^{\,2}$$

Using the method of determinants,

$$a = \frac{\sum_{i=1}^{n} \frac{y_i^2}{\sigma_i^2} \ln y_i \sum_{i=1}^{n} \frac{y_i^2}{\sigma_i^2} \ln x_i^2 - \sum_{i=1}^{n} \frac{y_i^2}{\sigma_i^2} \ln x_i \sum_{i=1}^{n} \frac{y_i^2}{\sigma_i^2} \ln x_i \ln y_i}{\sum_{i=1}^{n} \frac{y_i^2}{\sigma_i^2} \sum_{i=1}^{n} \frac{y_i^2}{\sigma_i^2} \ln x_i^2 - \left(\sum_{i=1}^{n} \frac{y_i^2}{\sigma_i^2} \ln x_i \right)^2}$$

$$b = \frac{\sum_{i=1}^{n} \frac{y_i^2}{\sigma_i^2} \sum_{i=1}^{n} \frac{y_i^2}{\sigma_i^2} \ln x_i \ln y_i - \sum_{i=1}^{n} \frac{y_i^2}{\sigma_i^2} \ln y_i \sum_{i=1}^{n} \frac{y_i^2}{\sigma_i^2} \ln x_i}{\sum_{i=1}^{n} \frac{y_i^2}{\sigma_i^2} \sum_{i=1}^{n} \frac{y_i^2}{\sigma_i^2} \ln x_i^2 - \left(\sum_{i=1}^{n} \frac{y_i^2}{\sigma_i^2} \ln x_i \right)^2}$$

The parameters were calculated and a power law function of the form $y = Ax^b$ was constructed for x-ray energies 1.4 to 8 MeV. **Figure 20** has three examples of the constructed power law function (red line) overlaid on the corresponding higher-energy spectral data (black crosses). The three successive plots show the emergence of the 4.8 MeV spectral peak above the higher-energy bremsstrahlung x-rays. The data points in or around the spectral peak (3.7 – 6.3 MeV) were not used to calculate the power law parameters for any spectra because they will be analyzed separately in the next section. The power fit in each subplot is higher in amplitude than it seems it should be by looking at the trend in the data. This occurred because the lower-energy points with higher flux values had smaller uncertainties than higher-energy points with lower flux values (see **Figure 17**). The least-squares method uses weighted data points such that the lower-energy points have more influence than the higher-energy points, thus bringing the fitted line up in amplitude.

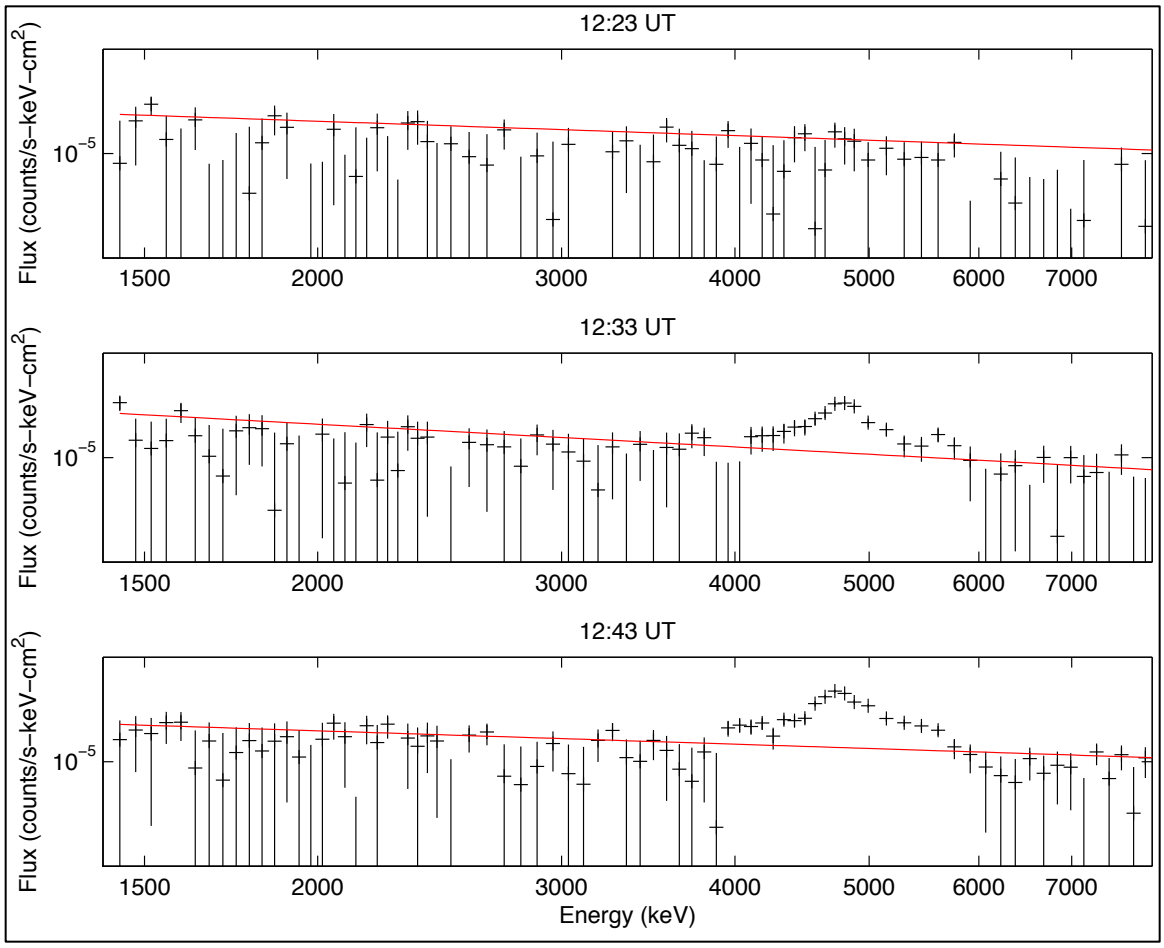

Figure 20. Three examples of higher-energy spectral data (black cross) and their corresponding power law fit (red line) at three consecutive times. The spectral peak data were not included in the fit.

The error associated with each of these power law parameters was calculated as described with the exponential errors. The errors are determined by:

$$\sigma_a^{\,2} = \frac{\sum_{i=1}^{n} \frac{y_i^{\,2}}{\sigma_i^{\,2}} (\ln x_i)^2}{\sum_{i=1}^{n} \frac{y_i^{\,2}}{\sigma_i^{\,2}} \sum_{i=1}^{n} \frac{y_i^{\,2}}{\sigma_i^{\,2}} (\ln x_i)^2 - \left(\sum_{i=1}^{n} \frac{y_i^{\,2}}{\sigma_i^{\,2}} \ln x_i \right)^2}$$

$$\sigma_b^{\,2} = \frac{\sum_{i=1}^{n} \frac{y_i^{\,2}}{\sigma_i^{\,2}}}{\sum_{i=1}^{n} \frac{y_i^{\,2}}{\sigma_i^{\,2}} \sum_{i=1}^{n} \frac{y_i^{\,2}}{\sigma_i^{\,2}} (\ln x_i)^2 - \left(\sum_{i=1}^{n} \frac{y_i^{\,2}}{\sigma_i^{\,2}} \ln x_i \right)^2}$$

The constructed power law and exponential function characterize the higher and lower energies of each spectrum respectively, and a combination of both functions characterizes the middle energies (200 keV – 1.4 MeV). Therefore, both functions were summed over all energies to create one function and the one function was overlaid on a full spectrum to confirm a good fit for the middle energies. **Figure 21** is one spectrum from later in the event (13:33 UT) when both spectral peaks are observed and flux is still elevated. The fitted function does not include the spectral peaks because they will be analyzed later. **Figure 21** shows that the combination of both functions is a good fit for the middle energies with the exception of the data points around the 350 keV spectral peak.

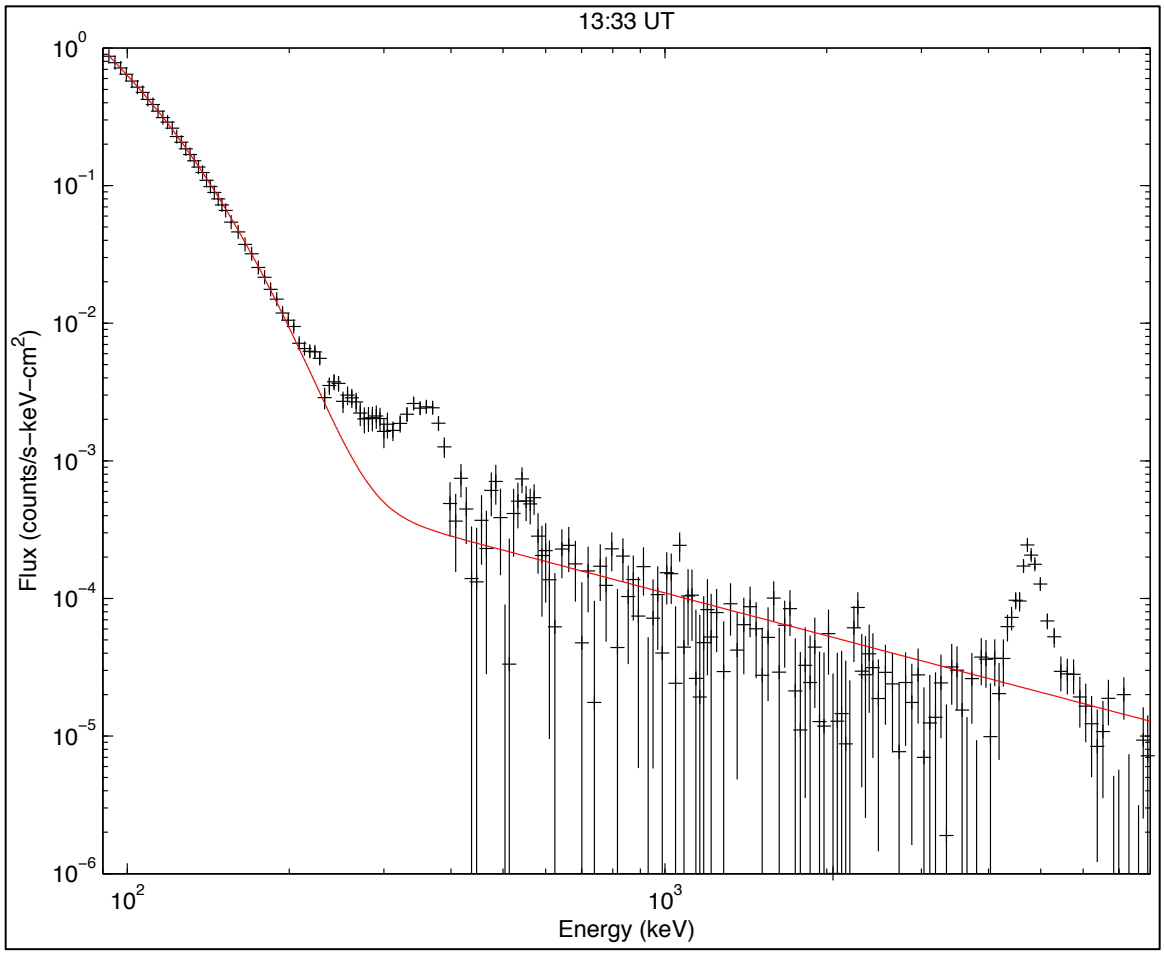

Figure 21. An example spectrum of the overall fit of the combination of a power law and an exponential function (red line) to the full spectral data (black crosses) at 13:13 UT. The spectral peaks at 350 keV and 4.8 MeV are not associated with the fit.

Now that each spectrum has been characterized by two functions, the temporal behavior of the spectra is contained in the four associated parameters. These parameters offer a simpler and more quantitative approach to analyzing the temporal characteristics of the spectra than trying to understand each data point individually. The parameters calculated were a and b for both an exponential function and a power law function. However, these parameters can be converted

into forms that are easier to compare with other data. The parameter a in each function was simply part of the whole coefficient A because $A = e^a$. It would be more practical to look at how the whole coefficient changes; therefore A is plotted instead for both functions. As discussed earlier, a common form of the exponential function used in electron precipitation analysis employs the value E_0 where $y = Ae^{-\frac{E}{E_0}}$. Therefore the b parameter from the exponential function was converted by $E_0 = -1/b$. A common form of the power law function is $y = Ax^{-b}$ because previous research has illustrated that the x-ray flux will always decrease with increasing energy, so a negative sign is assumed. Consequently the negative sign is divided out from the b parameter of the power law function. Each of these parameters was plotted as a function of time with error bars included. The analysis of each parameter is presented here.

The first parameter, A, which represents the amplitude of the exponential function that was fitted to the lower energy part of the x-ray spectrum (90 – 200 keV), is plotted in **Figure 22**. The error bars are plotted with each point, but they are small compared to the range of y-values, so they are sometimes hard to distinguish. For reference, uncertainties for all but four of the plotted points were below 10% of their calculated values. (The first two and last two values were exceptions, and had errors ranges equal to 20% of their calculated values.) The amplitude shown in the figure is an indication of the overall magnitude of the bremsstrahlung flux between 90 and 200 keV.

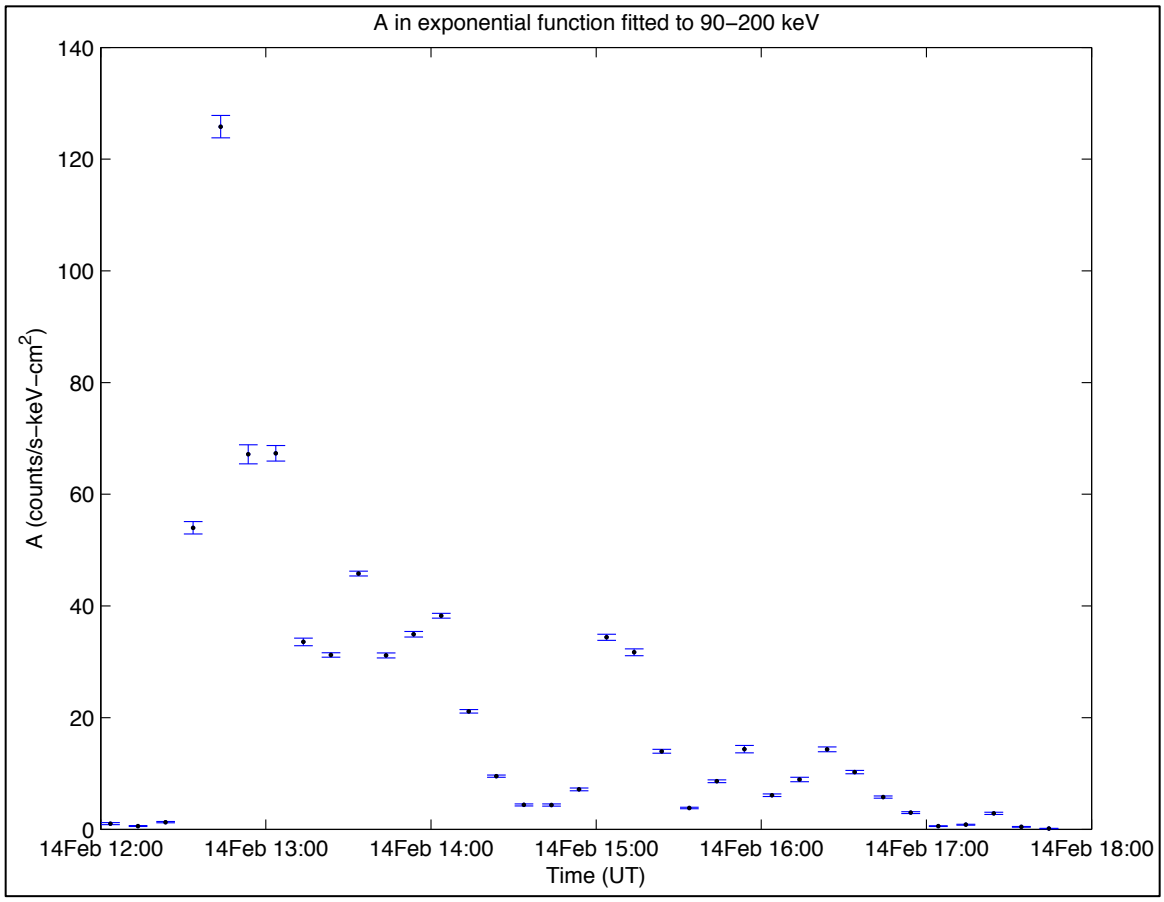

Figure 22. The amplitude of the exponential function fitted to 90 – 200 keV x-rays from each spectrum during the event.

Bjordal et al. [1971] observed lower-energy (from 30 to about 150 keV) electron precipitation from a balloon experiment during a substorm. The authors determined that precipitation directly related to a substorm should demonstrate an initial large impulse due to substorm onset, followed by a gradual decrease in flux during the recovery phase of the substorm. As explained earlier, the onset of the substorm that took place during February 14th event occurred around 12:30 UT, and the recovery phase lasted for several hours until 18:00 UT. The values of A show that an initial flux increase began some time around 12:33 UT and reached a peak at

approximately 12:43 UT. This spike was followed by a gradual decay in amplitude over the course of the event until its conclusion around 17:44 UT. The behavior of the lower-energy parameter A fits the criteria from *Bjordal et al.*, which means that the precipitation activity observed in the lower-energy part of the spectrum is directly related to the substorm.

The series of points shown in **Figure 22** also displays several local peaks at intervals of 30 to 60 minutes. This phenomenon has been addressed by *Hewitt* [2009] using the Piggyback flight fast spectra data. *Hewitt* compared THEMIS ground and satellite particle data with the fast spectra data and found that the variability is a result of substorm injections of plasma sheet electrons. *Hewitt* assumed wave-particle interactions as the precipitation mechanism, though THEMIS wave data was not examined to confirm this, nor is it the focus of this research.

Figure 23 is a time series of the e-folding energy E_0 during the event. The parameter E_0 is the exponent in the exponential function that characterizes the lower-energy part of the spectra. The parameter is a measure the steepness of a certain spectrum in the sense that higher values of E_0 mean a flatter spectrum because it takes more energy to decrease the flux by $1/e$. Conversely, the steeper the exponential function that characterizes the spectrum, the smaller the value of E_0 and the more lower-energy x-ray that are present relative to higher-energy x-rays (within 90 – 200 keV). The benefit of the parameter E_0 is that it quickly summarizes the distribution of x-rays without requiring an analysis of each bin. The data shown in **Figures 22** and **23** suggest an inverse relationship with A and E_0. The large amplitudes in A map to smaller values of E_0. This is evident in **Figure**

23, where points representing local maxima in **Figure 22** now appear as local minima.

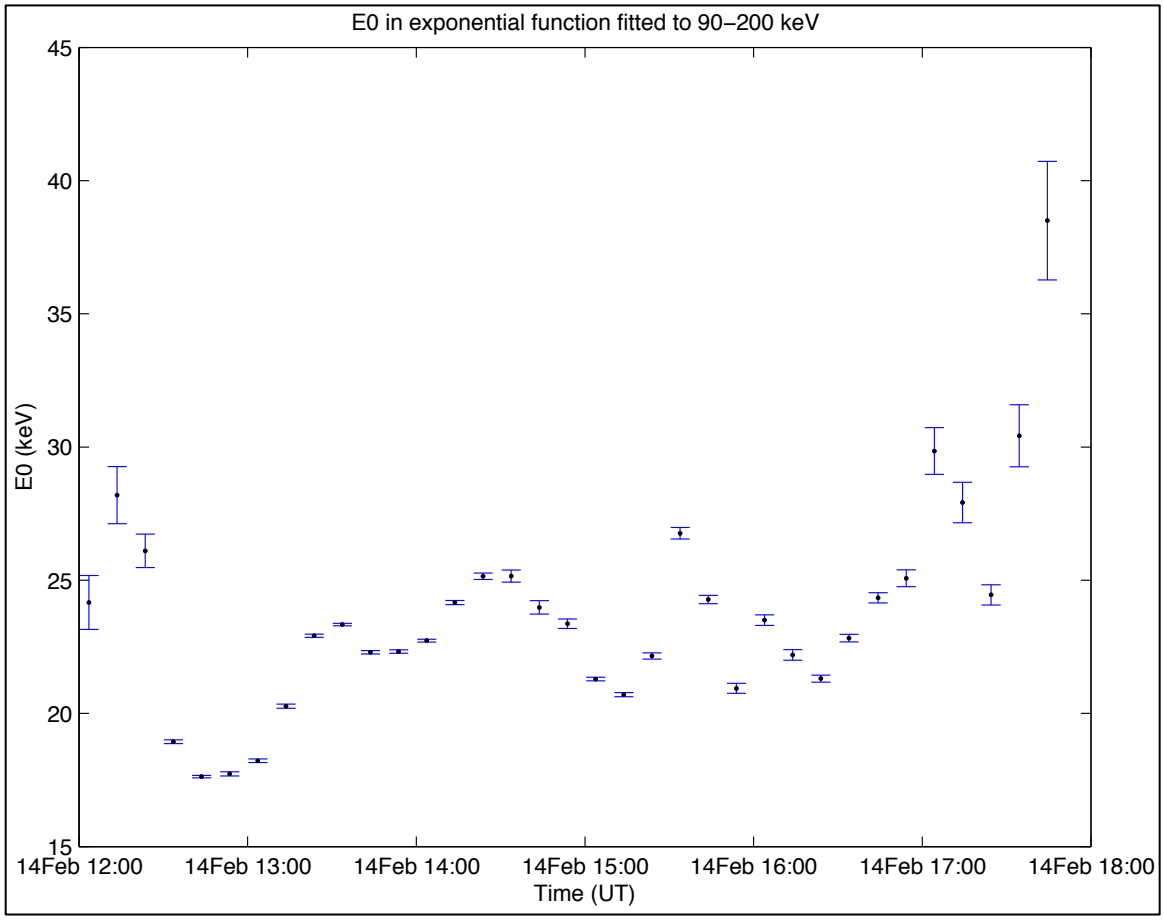

Figure 23. The e-folding energy from each exponential function fitted to part of each ten-minute-average spectrum from 90 to 200 keV during the event.

The quantities calculated during this event for E_0 are typical values found during previous balloon flights. *Barcus and Rosenberg* [1966] observed 15 to 150 keV x-rays and reported e-folding energies of 10 – 50 keV from several months'

worth of data, while *Smith et al*. [1995] observed e-folding energies of 15 – 45 keV from measured x-rays up to 300 keV during several quiet events.

One puzzling observation from **Figure 23** is the low value of E_0 at the onset of the substorm activity at approximately 12:30 UT. According to *Kangas et al*. [1975], higher-energy electrons should be observed at the beginning of the substorm because these are the electrons that are accelerated first. Those authors were observing x-ray energies in the 20 to 100 keV range, but the principle should still apply for the 90 to 200 keV energy range analyzed here. This would lead to an increase in E_0 as the spectrum displays a greater balance of higher-energy and lower-energy particles. However, as the figure shows, E_0 dramatically decreases at substorm onset, meaning that less energetic particles are dominating the spectra. The precipitation of higher-energy electrons may last no more than a few minutes; therefore two-minute-averaged, lower-energy x-ray spectra were constructed (not shown) with exponential fits to ascertain if this observation was also present in higher temporal resolution data. The e-folding energy for the two-minute spectra did slightly increase at onset before dramatically decreasing, but further data were studied to reach a more reliable conclusion.

Kangas et al. analyzed ratios between higher and lower energies to determine that higher-energy electrons were accelerated first. In order to evaluate the presence of higher-energy electrons in this event, the two-minute-averaged spectral data recorded were used to calculate similar ratios in both the lower-energy ranges discussed in *Kangas et al*., and the higher-energy ranges that are the focus of this study. These ratios are shown in **Figure 24a** and **Figure 24b**,

respectively. Both figures show an increase in higher-energy precipitation at onset, which means higher-energy electrons were accelerated first and precipitated first, as expected from *Kangas et al.*'s observations.

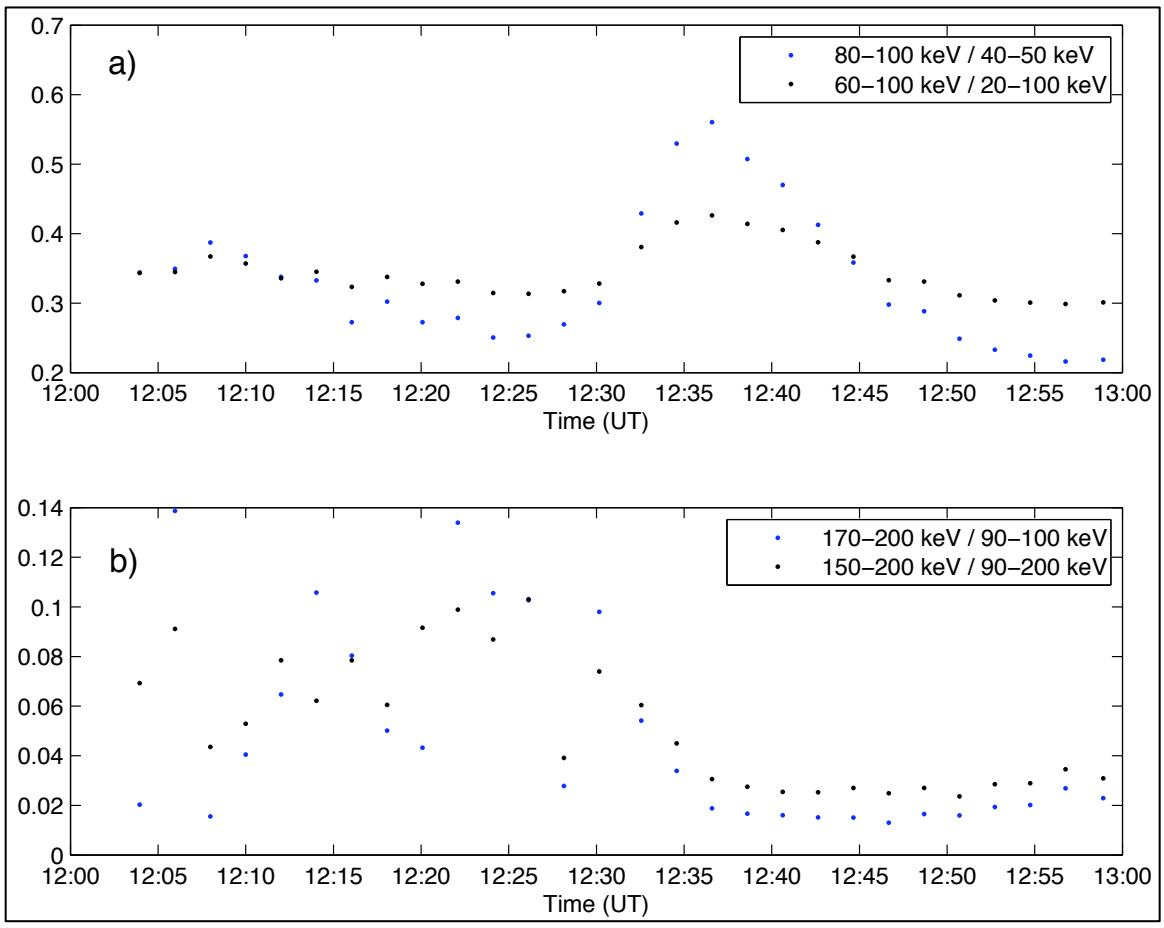

Figure 24. The ratios of certain energy ranges within the lower-energy x-rays during the first hour of the February 14th event using the two-minute-averaged spectral data.

Moving on to an examination of the higher-energy electron activity, **Figure 25** shows a time series of the amplitude of the power law function fitted to the higher-energy x-rays (1.4 – 8 MeV) observed during the event. Most of the data

points have large error bars, including one extremely large error at 13:13 UT that is not fully shown on the plot. At first glance, the figure suggests that the equation derived to calculate the amplitude error may be inaccurate because the error bars are too wide, suggesting the possibility of zero amplitude at each point. This would mean that only noise is being measured in this energy range and no actual precipitation activity is occurring. The actual x-ray counts collected at higher energies were analyzed to shed some light on this discrepancy.

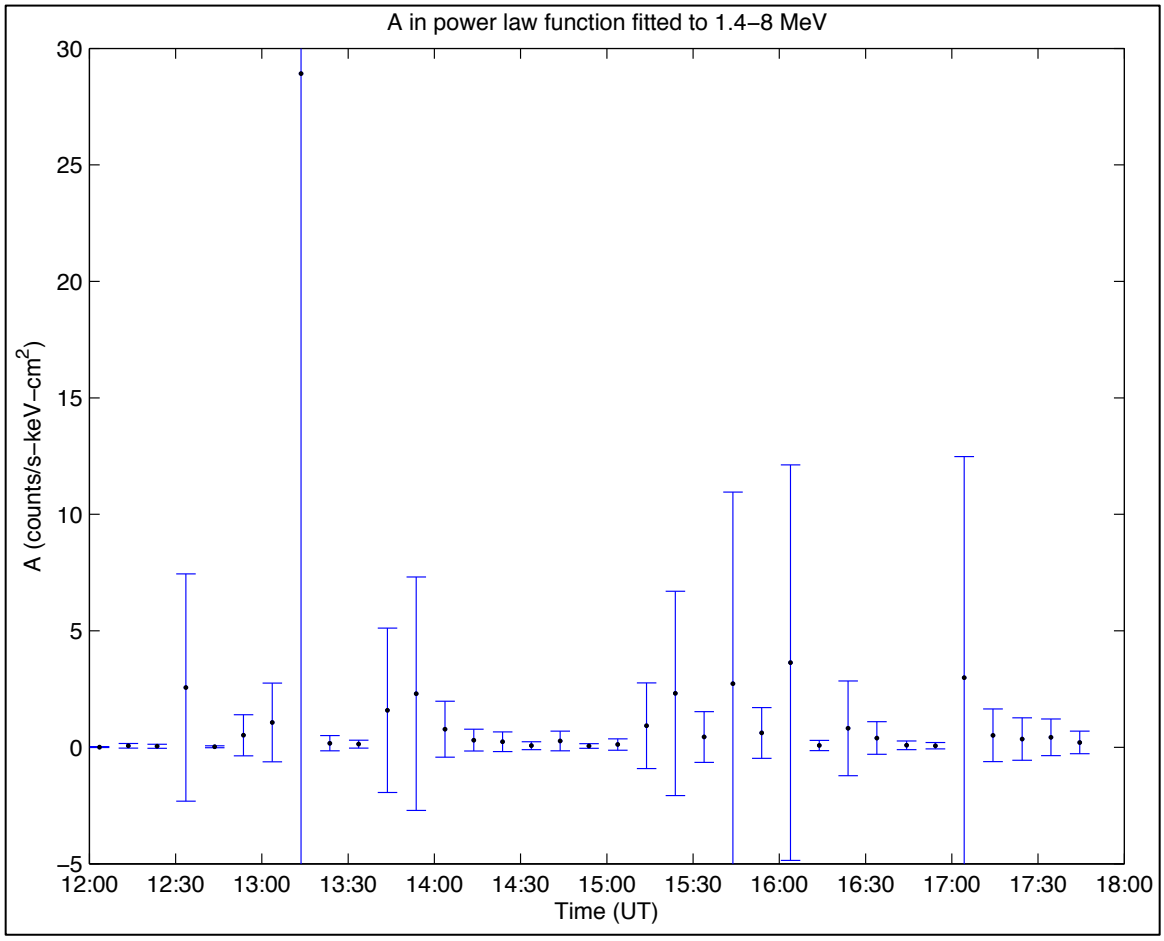

Figure 25. The amplitude of the power law function fitted to 1.4 – 8 MeV x-ray flux for each spectrum. Many of the error bars are large, suggesting a need for further examination to evaluate the accuracy of the data.

Figure 26 is a time series of x-ray counts summed over certain energies during the event. **Figure 26a** displays a sum of counts from 1.4 to 3.6 MeV from each ten-minute spectrum, while **Figure 26b** shows a sum of counts from 6.5 to 8 MeV in the same intervals. (Energies between 3.6 and 6.5 MeV were not included to avoid counting flux related to the 4.8 MeV spectral peaks in the spectra, which will be discussed later). The variance was calculated from the sum of squared uncertainties in each energy bin squared.

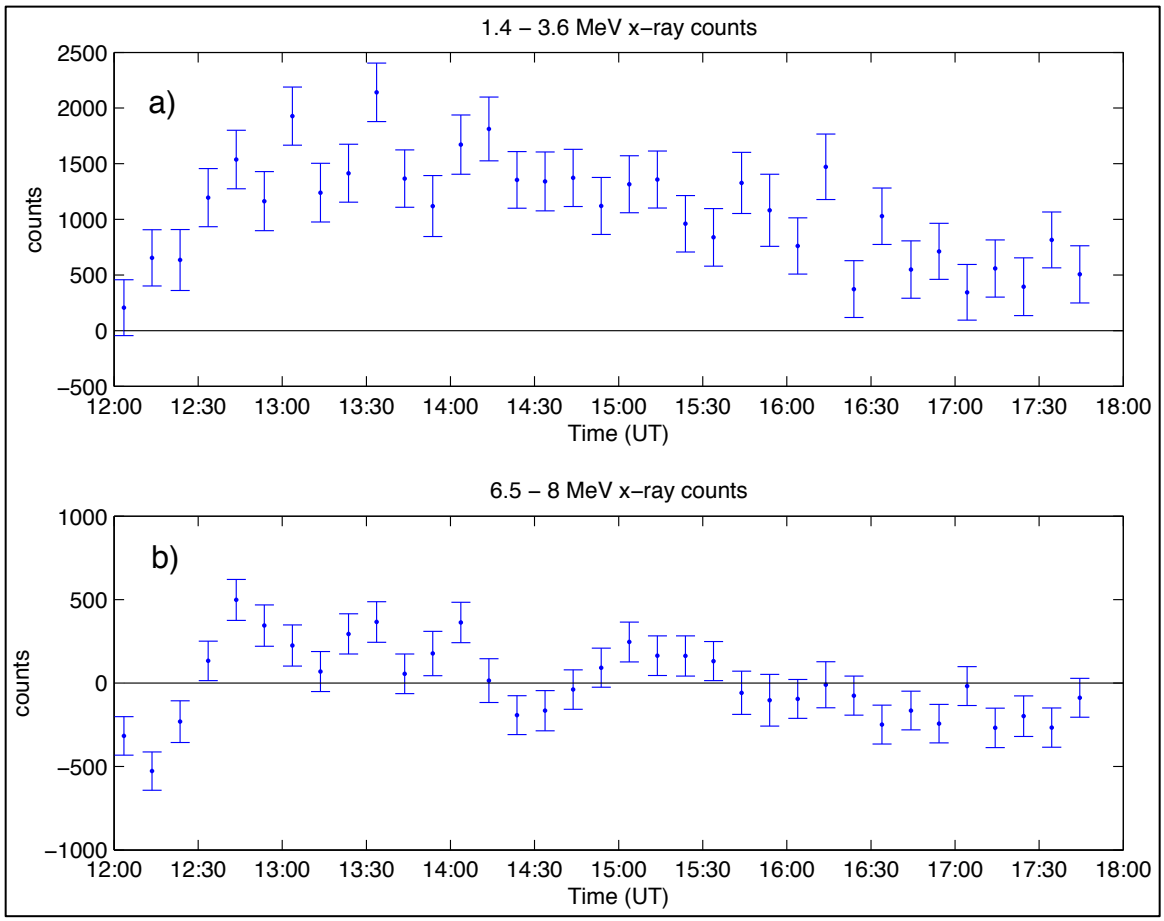

Figure 26. Sum of counts for each spectrum during the event for energies a) 1.4 – 3.6 MeV and b) 6.5 – 8 MeV.

The horizontal line through each subplot highlights a baseline of zero counts to provide perspective on the data points. **Figure 26a** shows that all counts in this energy range and their corresponding error bars are above zero except for the first point. In **Figure 26b**, 54% of the counts are below zero while 46% are above zero, which means the data could just be noise. While **Figure 26b** does suggest the counts measured in the highest energy range could be noise, the counts in **Figure 26a** do validate that the amplitude of the power law should not be zero. Consequently, the possibility of a miscalculation in the error bars in **Figure 25** cannot be ruled out. Since the source of any such miscalculation has not been discovered, the data shown in **Figure 25** will not be analyzed further until this discrepancy can be resolved.

Figure 27 is a time series of the power law exponent that characterizes the higher energy part of the x-ray spectra (1.4 to 8 MeV). Since the same assumptions were used to calculate the power law exponent and amplitude uncertainties, there may be discrepancies in these data shown in **Figure 27** as well. However, if it was assumed that the power law exponents and their corresponding uncertainties were correct, an analysis of substorm association can be performed. As stated in earlier sections, bremsstrahlung spectra for energies greater than 1.4 MeV have never before been characterized. As a result, there are no generally known criteria for

evaluating whether the observed higher-energy spectra are directly associated with the substorm or not.

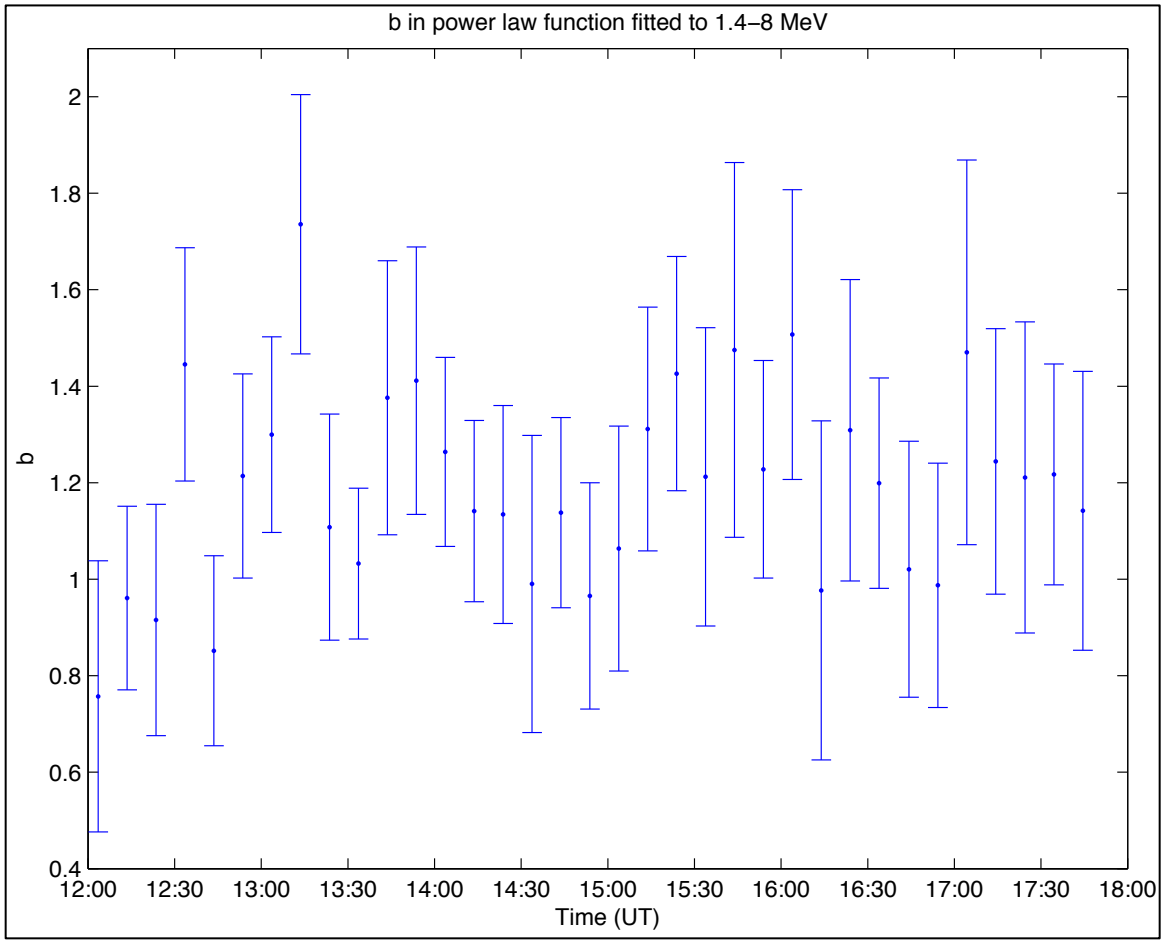

Figure 27. The exponent of the power law function fitted to x-ray energies 1.4 – 8 MeV from each spectrum.

Despite this fact, one attribute of substorm behavior can be checked using conclusions drawn from the lower-energy data. Substorm injections were the phenomenon proposed by *Hewitt* [2009] to have produced the 30- to 60-minute periodic peaks in the lower-energy data. The higher-energy data can be analyzed to

confirm whether the same periodicity exists from the lower-energy data. This conclusion will show whether some of the higher-energy precipitation was a result of substorm injections also. A quantitative analysis to determine the presence of substorm injections is outlined here.

E_0 is analogous to b in that their values correspond to the steepness of the line fitted to the data. If the substorm injection periodicity evident in the e-folding energy E_0, then some periodicity should appear in the power law exponent as well if substorm injections are present. Thus, the parameters E_0 and b can be compared to ascertain if the 30- to 60-minute periodic peaks present in the e-folding energy are present the power law exponent b.

A linear-correlation analysis can be performed to determine exactly how closely these parameters are correlated. *Bevington and Robinson* [2003] states that the correlation coefficient can determine whether the variations observed in one value are correlated with the variations in another value. The coefficient ranges from -1 to +1, where 0 represents no correlation, and values near positive or negative 1 indicate a strong (direct or inverse, respectively) correlation between the variables. The correlation coefficient between E_0 and b here was determined to be 0.1. According to *Bevington and Robinson*, this is a very low correlation coefficient, indicating with confidence that any patterns in the two data sets are not closely linked. This finding demonstrates that the periodicity observed in the lower energies is not present in the higher energies and confirms that the substorm injections did not include MeV energies. In fact, there is not much change in the higher-energy x-rays during the substorm at all.

Estimation of Parent Electron Spectrum

The spectrum of the original electrons precipitating from the outer radiation belt can be inferred from the observed x-ray spectrum. Low-orbiting satellites can directly measure the flux of precipitating electrons, but cannot measure a particular area long enough to build up a spectrum in the way that a balloon can. However, inferred parent electron spectra can be compared with satellite data measurements of electron activity to confirm that the calculated spectra are correct. The inferred electron spectrum offers more insight into what source mechanisms are at work.

As described previously, precipitating electrons interact with atoms in the atmosphere to create bremsstrahlung radiation. The bremsstrahlung x-rays then experience Coulomb scattering and some atmospheric absorption before reaching the height of the balloon. These processes undergone by these x-rays are very difficult to due to their complexity, though advanced computer models (such as the Geant4 code referenced in *Makhmutov et al*. [2006]) are sometimes employed in an attempt to accurately simulate the production of x-rays from a given electron spectrum. Unfortunately, implementing these codes can be somewhat difficult and time-consuming. This paper, instead, present an alternative approach to estimating the electron spectra using previously published research.

Berger and Seltzer [1972] utilized a Monte Carlo model to calculate the transport of electrons and photons through the atmosphere and developed a relation between the precipitating electron spectrum and the resulting x-ray spectrum for various atmospheric depths. The authors assumed mono-energetic electron beams precipitating with isotropic angular distribution pointing down, and

also that the precipitation occurred over a sufficiently wide area that the only spatial variable was atmospheric depth. They summed their results into tables relating mono-energetic electron beams to the x-ray spectrum created at specific atmospheric depths. **Table 2** is a reproduction of the *Berger and Seltzer* table for atmospheric depths of 6 to 7 g cm^{-2}. The values inside the table correspond to the number of x-rays created at each energy k (rows) from one electron at energy T_0 (columns). The blank spaces in the table refer to photon energies that cannot be created by the specified electron because the energy of bremsstrahlung radiation produced by precipitation cannot be higher than the energy of the original electron.

Table 2. The number of photons created at each photon energy k (keV) from the mono-energetic beam with electron energies to T_0 at 6 – 7 g cm^{-2}.

T_0 (keV) k (keV)	2000	1000	500	200	100	50	30
20	3.0E-05	1.0E-05	3.4E-06	8.0E-07	2.7E-07	9.1E-08	2.3E-08
30	3.8E-04	1.6E-04	6.1E-05	1.6E-05	5.2E-06	8.0E-07	
40	9.5E-04	3.4E-04	1.1E-04	2.4E-05	6.6E-06	3.3E-07	
50	1.1E-03	3.8E-04	1.2E-04	2.0E-05	4.0E-06		
60	9.1E-04	3.1E-04	9.4E-05	1.5E-05	2.2E-06		
80	6.0E-04	1.9E-04	5.5E-05	7.8E-06	3.3E-07		
100	4.0E-04	1.3E-04	3.4E-05	3.9E-06			
150	1.9E-04	5.5E-05	1.2E-05	6.3E-07			
200	1.1E-04	2.9E-05	5.6E-06				
300	5.0E-05	1.1E-05	1.4E-06				
400	2.9E-05	5.1E-06	3.0E-07				
500	1.8E-05	2.5E-06					
600	1.2E-05	1.3E-06					
800	6.1E-06	3.0E-07					
1000	3.4E-06						
1500	6.9E-07						

Table 2 can be used to construct original electron spectra from the measured x-ray spectra during the February 14th event. However, the BARREL Piggyback slow spectra data collects x-rays into much narrower energy bins than are displayed in the rows of the original table. Additionally, the onboard x-ray detector measures energies in numerous bins beyond the energy of those shown in the original table. These facts necessitate that the original table be expanded in both its rows and columns to accommodate the energy ranges measured by the x-ray detector. A method was developed to interpolate intermediate data values within the table to and extrapolate additional values beyond the current table limits in order to obtain the x-ray electron energies of interest.

The method was derived from a plot of the *Berger and Seltzer* data. The data in **Table 2** are plotted in **Figure 28**, but the photon energies have been normalized, meaning photon energy is plotted on a scale of 0 to 1 as a fraction of the parent electron energy. The data were plotted in this way to reflect the fact that fewer and fewer x-rays are possible as photon energy approach the energy of the parent electron. In other words, the number of x-rays produced must be zero in all cases when normalized k is 1.

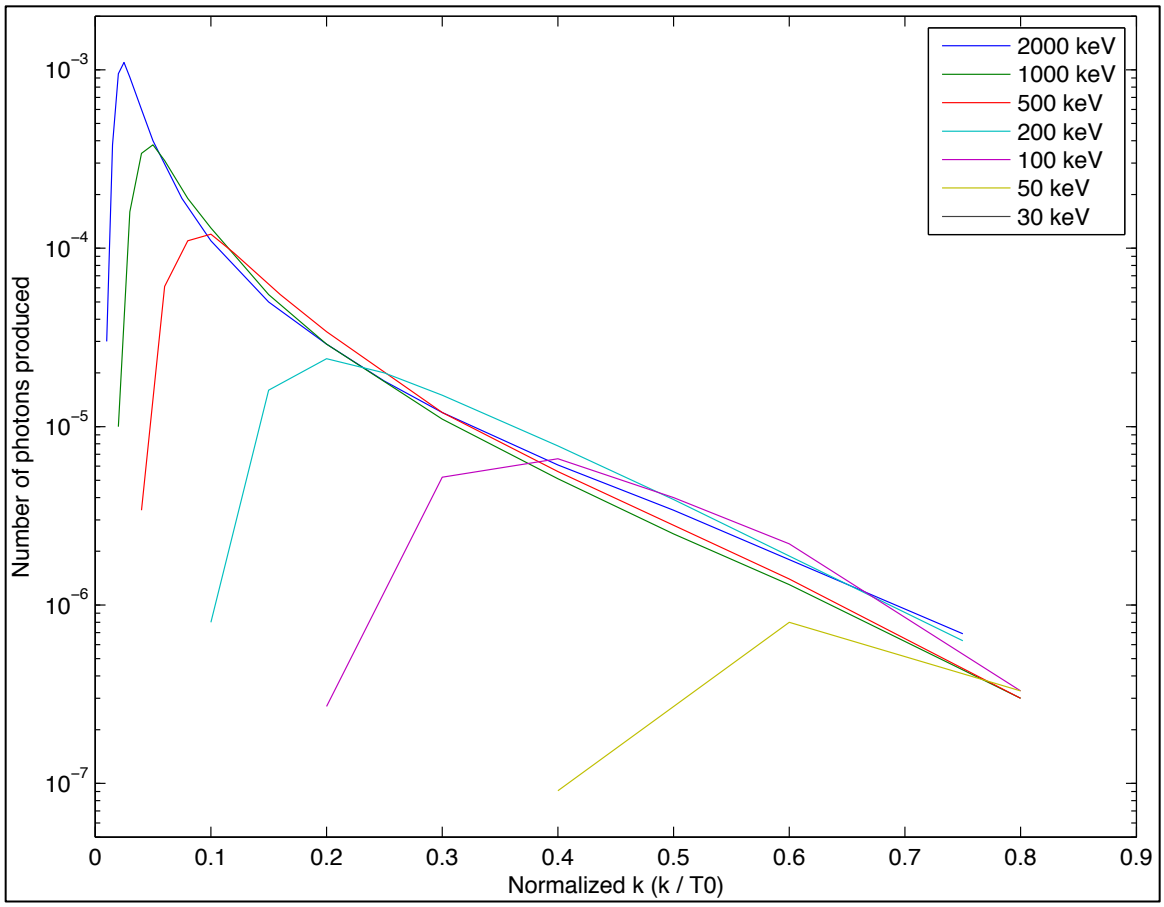

Figure 28. The number of photons produced at each normalized photon energy from one electron at a particular energy. Each line corresponds to different electron energies, except 30 keV, which is just one point from **Table 2**.

The numbers of x-rays produced at the mid-point of each energy bin from the measured x-ray spectra (ranging from 90.2 keV to 1.97 MeV) were interpolated from the lines in **Figure 28**. The available electron energies were also expanded by interpolating for electron energies between 100 keV and 2000 keV with a step size of 50 keV.

Some assumptions were made to obtain photon and electron energies higher than 2000 keV. **Figure 28** shows that (moving from right to left) the lines

representing each electron energy all lie along the same line. However, each electron energy line reaches a point where its y-value peaks and begins to decline. For example, the y-values of the 100 keV line follow the same path as the higher electron energy lines until the line reaches a normalized k-value of 0.4 (or 40 keV, in this case), after which, the y-values start to decrease. This pattern leads to an assumption that the lines for electron energies above 2000 keV will follow the same path as the 2000 keV line until the point where the 2000 keV line turns downward. The 2000 keV line begins to decline at an x-value of approximately 0.025 (equivalent to 50 keV), but to be conservative, only points at normalized k-values of 0.08 and above were used for extrapolation to higher energies. Therefore, the numbers of x-rays produced were interpolated along the 2000 keV line for electrons with energies greater than 2000 keV. The electron energies were only extended up to 5 MeV and since 0.08 of 5 MeV is 400 keV, the smallest x-ray energies that were obtained were 400 keV.

Part of the expanded table can be seen plotted as a surface in **Figure 29**, which covers electron energies from 500 to 5000 keV and x-ray energies between 400 keV and 3650 keV. The black dots plotted on the surface are the original points from the *Berger and Seltzer* table. These points fall on the surface, as should be expected from a correct interpolation. Only part of the table was plotted to highlight the position of the original points with respect to the surface.

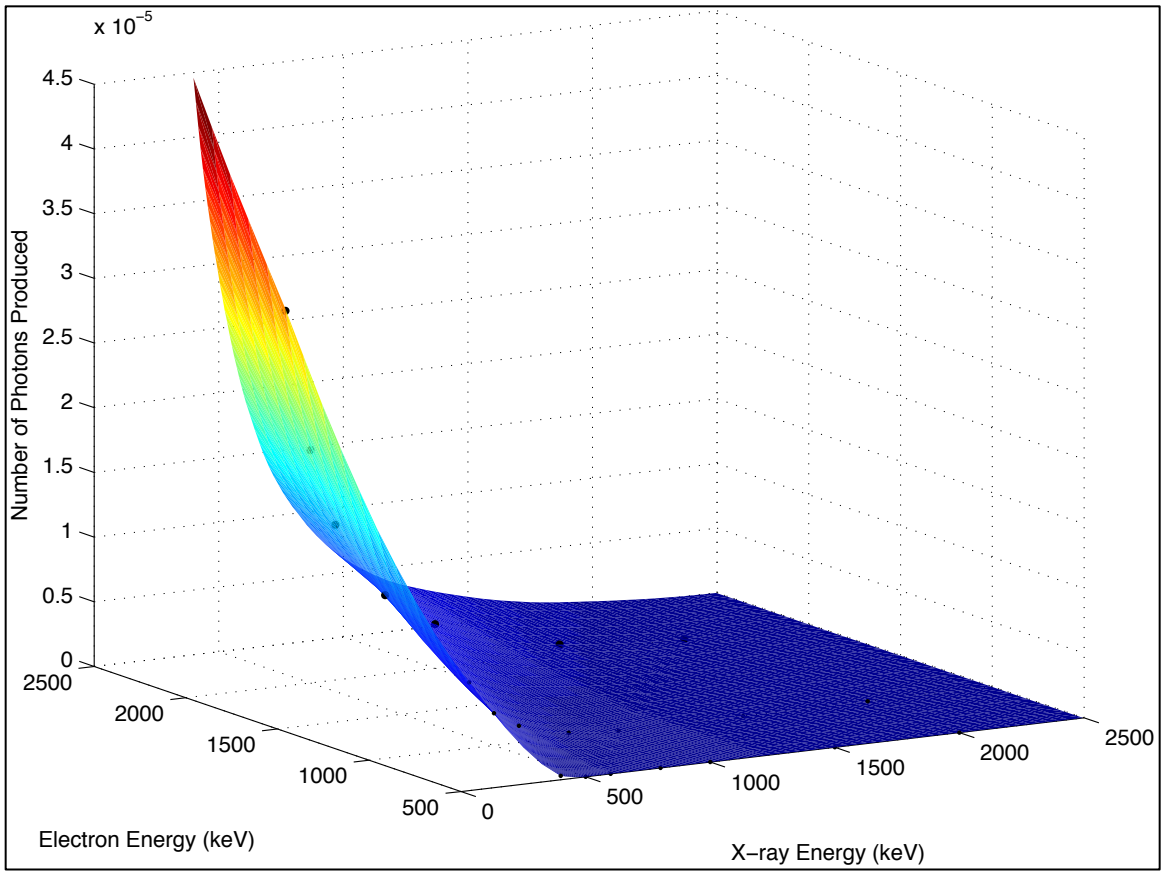

Figure 29. Part of the expanded *Berger and Seltzer* table plotted as a surface with the original points overlaid as black dots.

The expanded table was used to solve the linear system $A \times X = B$, where A is the expanded table with units of keV^{-1} and B is a vector of the measured x-ray spectrum with units of counts s^{-1} keV^{-1}. X is a non-negative vector representing the (unknown) number of electrons at each energy (in other words, the electron spectrum) with units of counts s^{-1}. The measured x-ray spectrum had previously been corrected for losses due to the atmosphere; however because the *Berger and Seltzer* table already accounts for these losses, the x-ray data used corrected for detector losses only.

Two methods were used to calculate the electron spectrum using the expanded table. One method involved assuming the electron population was one or more mono-energetic beams, while the other method assumed a power-law distribution for the electron population. The first method comprised of solving for the vector X using built-in MATLAB functions. The vector X in the linear system was calculated by finding the least-squares non-negative solution (since the system was underdetermined and no unique solution existed). The value of X was calculated for each ten-minute-averaged spectrum from the February 14th event. For example, this method indicated that the measured x-ray spectrum at 12:33 UT was produced by three mono-energetic electron beams at 600 keV, 1300 keV, and 4650 keV. The x-ray spectrum calculated from the mono-energetic beams and compared with the observed x-ray spectrum has a chi-squared value of 120. This is the lowest observed chi-squared value because the vector X is the least-squares solution.

The second method comprised of constructing the vector X from a power-law function ($y = Ax^b$) and testing different values for the parameters A and b. The values of A that were explored ranged from .01 to 10^{10}, while the values of b ranged from -0.1 to -3.5. The constructed spectrum was multiplied by the extended *Berger and Seltzer* table to produce an x-ray spectrum. This spectrum was compared to the observed x-ray spectrum at 12:33 UT in an effort to obtain the fit with the lowest chi-squared value. However, because the system was underdetermined and there was no unique solution, hundreds of power-law functions (with different amplitudes and exponents) produced x-ray spectra that had the same chi-squared value of approximately 123. Some of the results are summarized in **Figure 30**

where the values of chi-squared (from 120 to 200) are plotted as contours with their respective amplitudes and exponents.

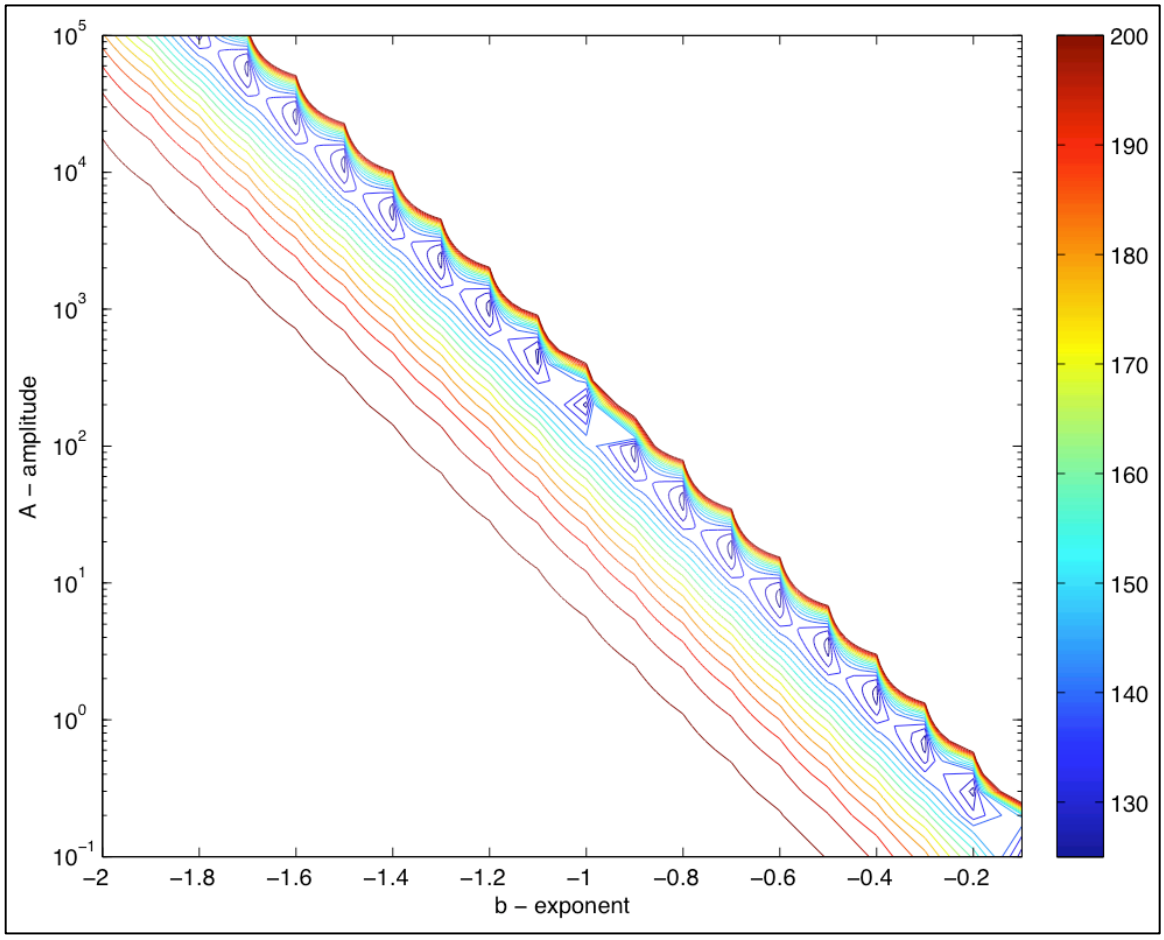

Figure 30. The values of chi-squared at different values of amplitude and exponent from the power-law function. Many different values of A and b produce the same chi-squared value. The color bar is the value of chi-squared.

The observed x-ray flux at 12:33 UT is plotted in **Figure 31** along with the x-ray fluxes calculated from the two electron spectra (the mono-energetic beams and selected power-law fits) using the expanded *Berger and Seltzer* table. The blue line is the calculated flux from the mono-energetic beams, while the red and the green

lines are examples of fluxes calculated from two power-law fits with the same chi-squared value. The green line is the calculated x-ray flux from the power-law fit with the largest value of b used ($y = 0.13x^{-0.1}$), while the red line is the fit with the smallest b-value ($y = 7.33x10^{9}x^{-3.2}$). The lines show that the two methods agree on a similar fit for the lower-energy x-rays (400 – 1000 keV), but all lines produce different results at higher energies (1 – 3.6 MeV).

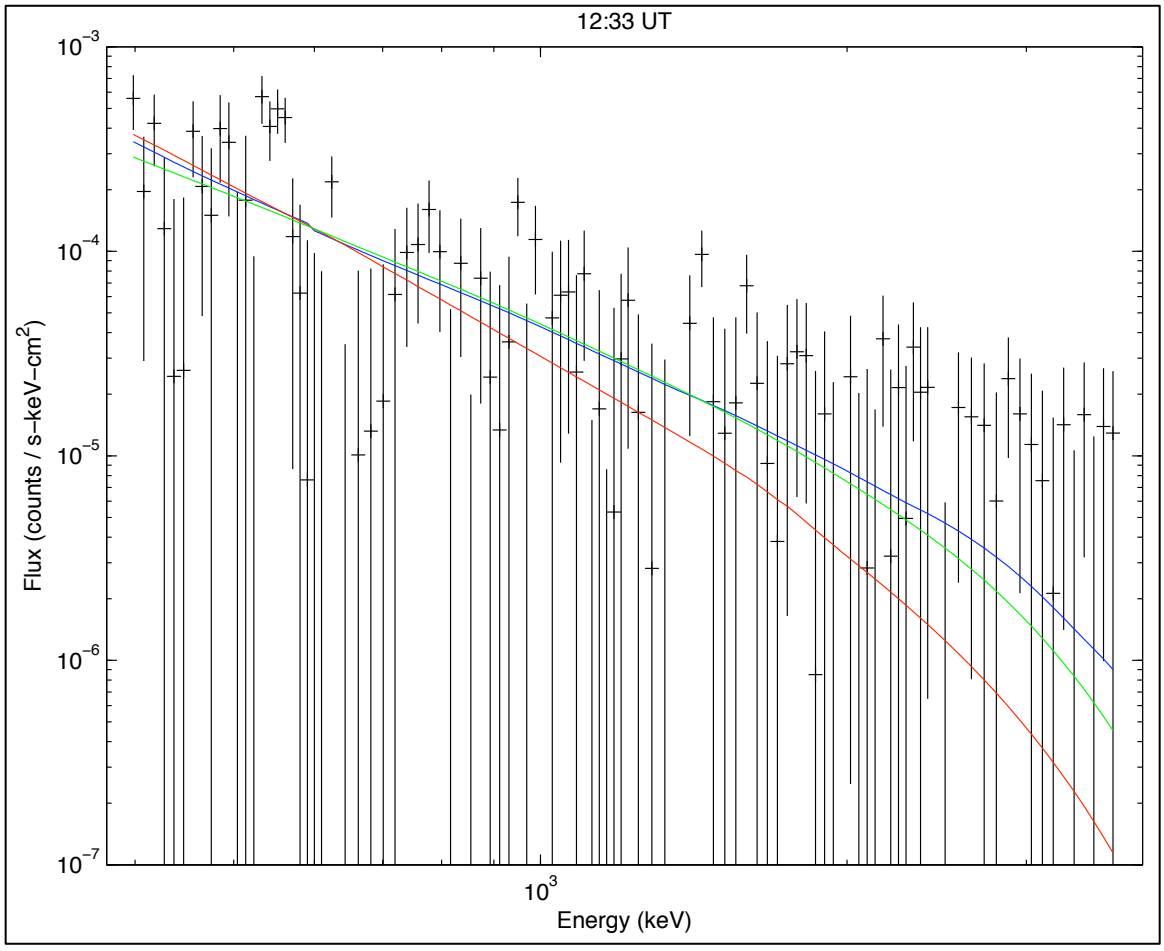

Figure 31. The observed x-ray fluxes (black crosses and lines) from 400 to 3600 keV at 12:43 UT and the calculated x-ray fluxes from one mono-energetic source (blue line) and two power-law fits (red and green lines).

The two methods used to calculate the electron spectrum produced hundreds of different solutions for the x-ray spectrum at 12:33 UT on February 14th, each within 3% of the same chi-squared value. Since many solutions are viable, comparison with direct measurements of these electrons can provide limitations on what are actual solutions. For example, the electron fluxes calculated from the electron spectra should be similar to the precipitating electron fluxes measured by spacecraft. Satellite data were compared to the range of possible solutions to identify which of the calculated electron spectra agreed with the observed data best.

The Solar Anomalous and Magnetospheric Particle Explorer (SAMPEX) is a low-altitude (~600 km), polar-orbiting satellite that measures energetic particles. Two of the instruments onboard SAMPEX measure electrons in the energy range of interest. The Heavy Ion Large Telescope (HILT) sensor measures not only heavy ions, but also electron count rates in two channels. The first channel measures electron with energies greater than 150 keV and the second measures energies greater than 1 MeV [*Blake et al*., 1996]. The second useful instrument is the Proton/Electron Telescope (PET) that measures, among other things, count rates of electrons with energies greater than 500 keV [*Cook et al*., 1993].

The SAMPEX spacecraft passed within the area of the Piggyback balloon during the February 14th event. One conjunctions occurred between 12:40 and 12:50 UT. The geographic coordinates of SAMPEX and the balloon at this time are plotted in **Figure 32**. SAMPEX coordinates are determined by the location of the foot point of the magnetic field line SAMPEX is on at each interval. The balloon's

location is labeled by the red dot. The balloon moves slowly enough that its position may be assumed to be stationary over the ten-minute period.

It is worth noting that, as seen in **Figure 32,** the balloon and the spacecraft were about 40 degrees in longitude away from each other during the time period specified. However, as *Brown et al*. [1965] pointed out, electron precipitation during a substorm has a large longitudinal extension. *Brown et al.* reported a precipitation area extending past the 20 degrees longitude difference of their two balloon locations.

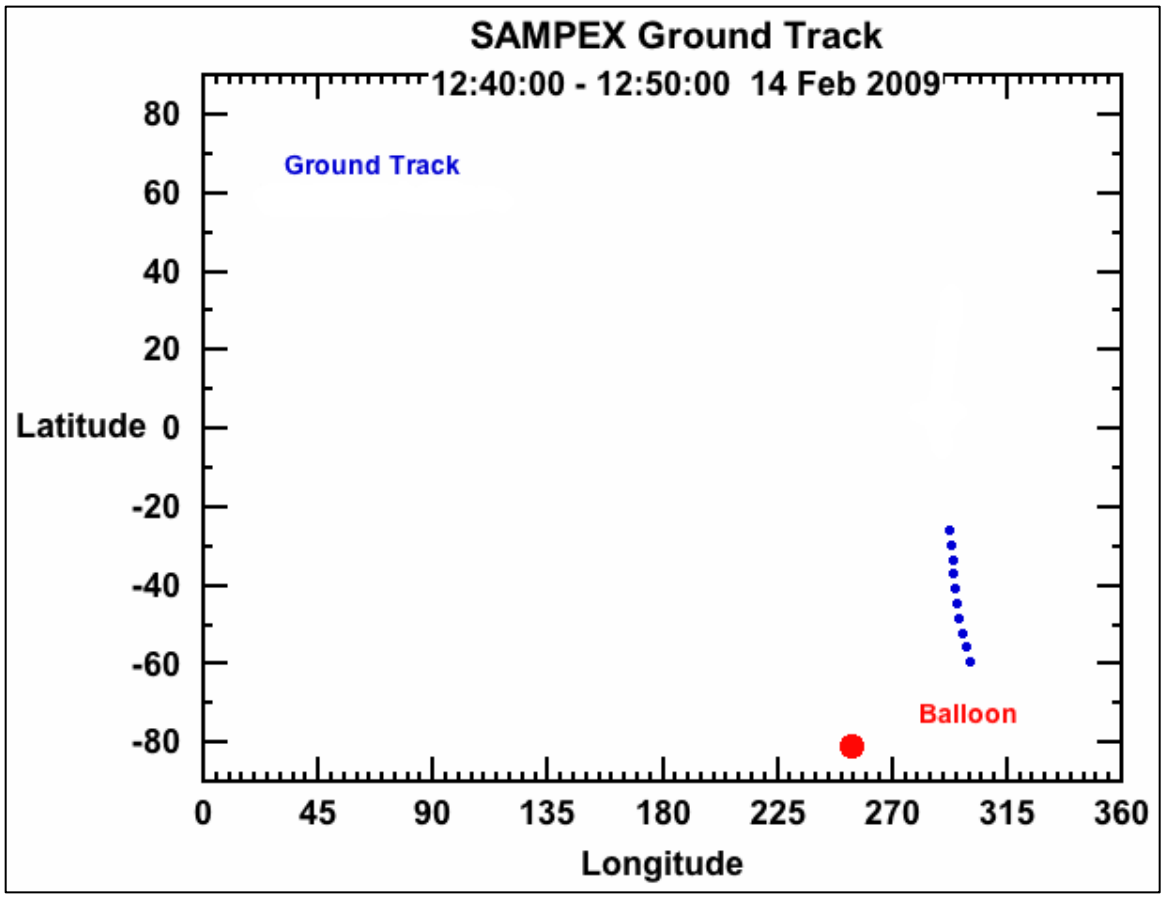

Figure 32. The geographic coordinates of the balloon and SAMPEX during one conjunction [Image provided by J. B. Blake, 2009].

Between 12:40 and 12:50 UT, the HILT and PET instruments observed an increase in count rates of precipitating electrons and this data are displayed in **Figure 33**. The calculated latitude, longitude, and L-shell values are also plotted for reference. The HILT channel that is shown measures electrons with energies greater than 1 MeV, while the PET channel measures electrons above 500 keV. The count rate profiles are ragged because the spacecraft is spinning at a rate of one rotation per minute. Additionally, the HILT instrument has a larger viewing area (100 cm^2 sr) than the PET instrument (10 cm^2 sr).

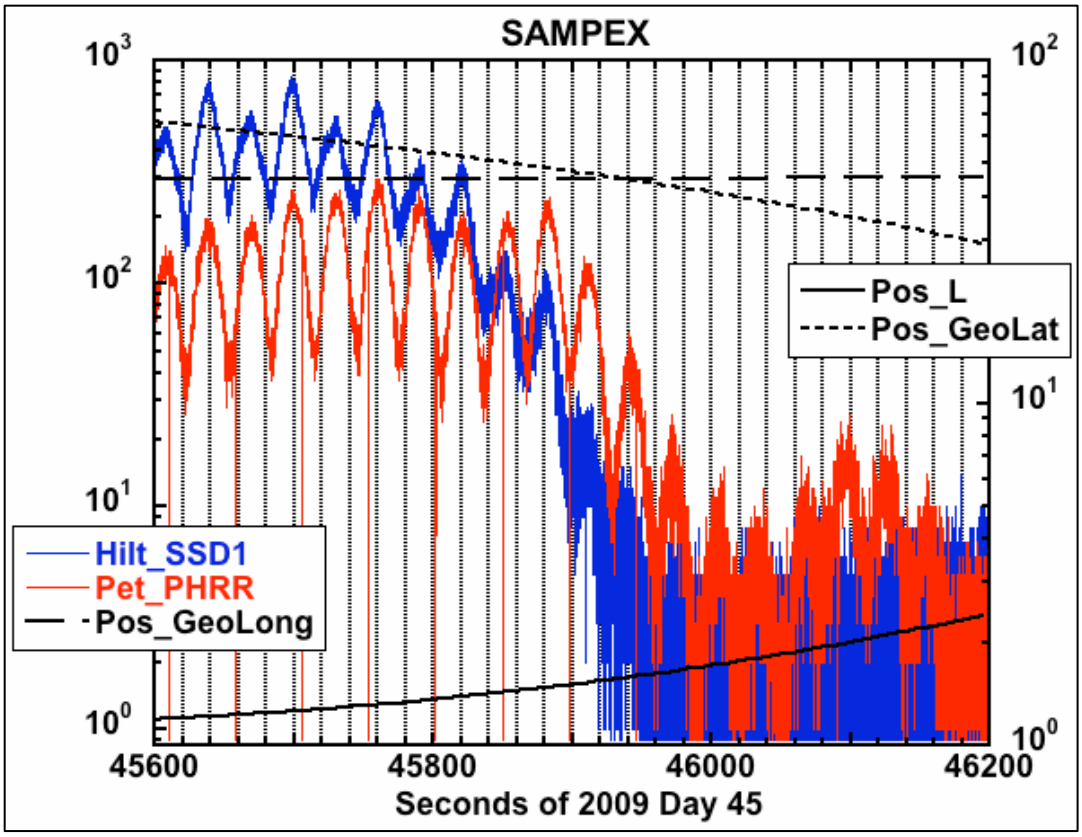

Figure 33. HILT (blue line) and PET (red line) measurements of precipitating electrons from 12:40 UT (45600 seconds) to 12:50 UT (46200 seconds). Latitude, longitude, and L-shell values (black lines) are also plotted [Image provided by J. B. Blake, 2009].

SAMPEX and balloon data were compared at 12:40 UT because this time corresponded to the point of closest approach between the two platforms were during the ten-minute interval of SAMPEX data. The inferred electron spectra was thus drawn from the x-ray spectrum beginning at 12:33 UT because this ten-minute average included the measurements made at 12:40 UT. The electron count rates from the HILT and PET instruments were estimated from **Figure 33**. In order to compare the calculated electron spectra with the observed electron count rates from SAMPEX, all data were converted into electron fluxes. The fluxes from SAMPEX were calculated by dividing the observed count rates by each of the instrument's viewing area and the inferred electron count rates were divided by the balloon's viewing area (364 cm^2 sr). With regard to the mono-energetic beam electron population solution, the fluxes all three beams were summed to compare to the PET data, while only the fluxes from the 1300 keV and 4650 keV beams were used for comparison to the HILT data. The data are summarized in **Table 3**. The range of fluxes calculated for electron above 500 keV electrons and electrons above 1 MeV electrons from all power-law fits within a 3% chi-squared range are listed in **Table 3** as well.

Table 3. The measured and calculated count rates and fluxes from SAMPEX and the balloon at 12:40 UT.

2/14/09 12:40 UT	Flux (counts s^{-1} cm^{-1} sr^{-1})
PET	15
Least-squares >500 keV	11.8
Power-law fit >500 keV	10.47 – 0.74
HILT	5
Least-squares >1 MeV	0.92
Power-law fit >1 MeV	2.22 – 0.65

Table 3 shows that the calculated electron fluxes from the mono-energetic beams and from the possible power-law fits are lower than expected from the SAMPEX measurements. The mono-energetic beam solution is within 20% of the flux measured by the PET instrument, but is lower by a factor of 5 when with the HILT measurement. The fluxes from the power-law fits are all too low to make any assumptions that might allow the elimination of some of the hundreds of solutions. Interestingly, the calculated fluxes from one power-law fit do maintain the ratio between the HILT and the PET fluxes (ratio of 3). The power-law function $y = 3.27x10^{7}x^{-2.5}$ produces x-ray fluxes of 5.17 for electron energies greater than 500 keV and 1.72 for electron energies greater than 1 MeV. However, this observation is not conclusive, and without further information, it appears that the true electron spectrum cannot be reliably determined by either of the two methods applied here.

Analysis of Spectral Peaks

As described above, the x-ray data recorded by the BARREL Piggyback flight revealed the presence of two spectral peaks at energies of 350 keV and 4.8 MeV. These authors have never before observed similar peaks at these energies, thus the goal of this section is to provide insight into the source of these peaks. It is first important to note that the spectral peaks cannot be a product of electron precipitation because the bremsstrahlung creation, scattering, absorption processes in the atmosphere broadens the spectrum of x-rays generated by a single precipitating electron at any given energy. Since electron precipitation has been ruled out, another potential source, precipitating high-energy protons, is discussed.

To begin, two different Gaussian functions ($y = ae^{-\frac{(x-b)^2}{2c^2}}$) were fit to the spectral peaks in an effort to analyze their temporal behavior. These Gaussians were combined with the exponential and power law functions and plotted as one line over the spectral data as seen in **Figure 34**. The plot shows that the Gaussian functions are a good representation of the data points associated with the spectral peaks. The amplitude parameters a from the Gaussian functions can be used to analyze the temporal behavior of the peaks.

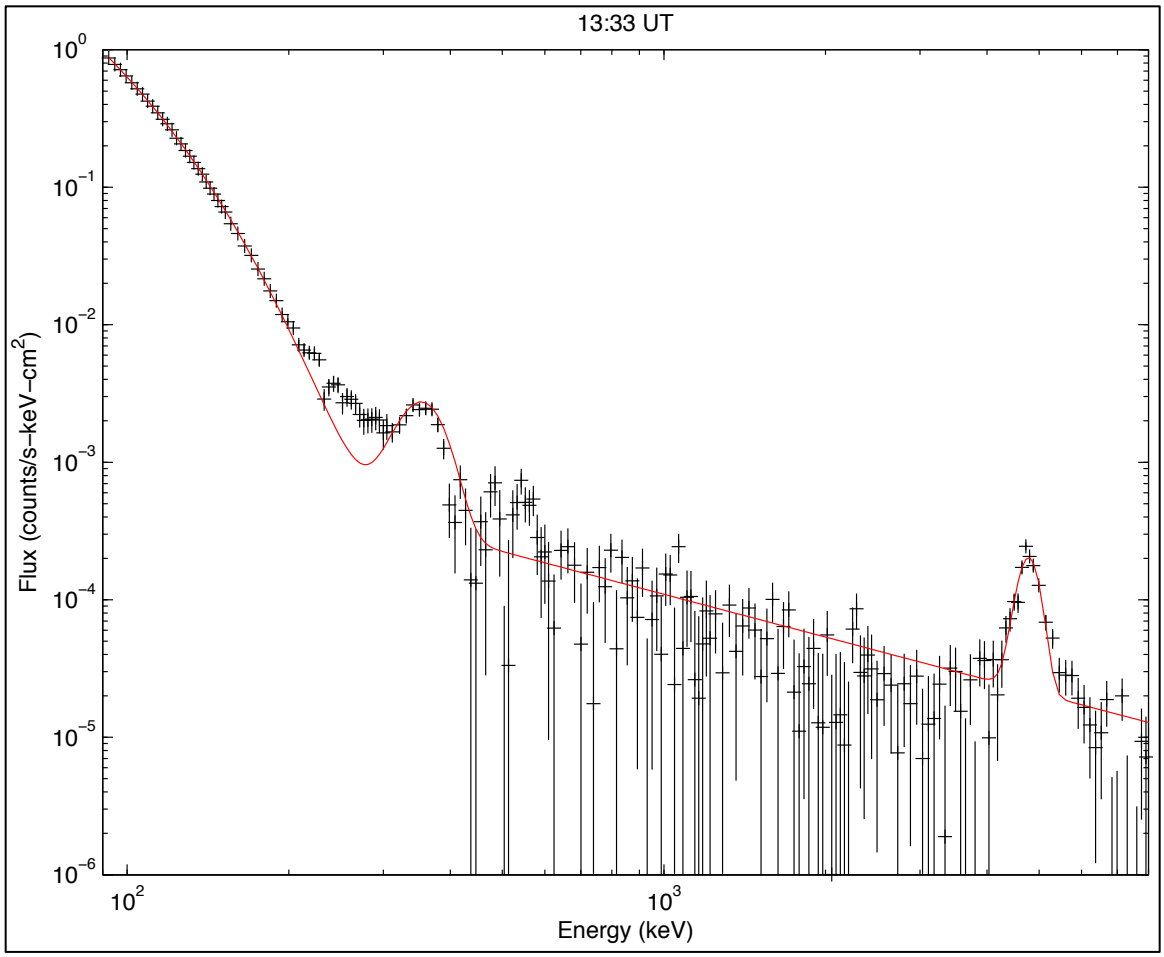

Figure 34. A multi-function (exponential, power law, and Gaussian) fit (red line) overlaid on the averaged flux observed and their calculated uncertainties at 13:33 UT (black crosses and lines).

The amplitudes a of both Gaussian functions are plotted with error bars as a function of time in **Figure 35**. During the event, the spectral peaks were not observed in some spectra so a Gaussian was not fit to any data. In these cases, the amplitudes are plotted as zero. This plot shows that the amplitudes are highly correlated, with both peaks first appearing at 12:33 UT before disappearing around 14:30 UT and then re-appearing at 14:54 UT. The linear correlation coefficient of

the two amplitudes is 0.93. The high correlation between the two amplitudes suggests that the spectral peaks have the same source mechanism.

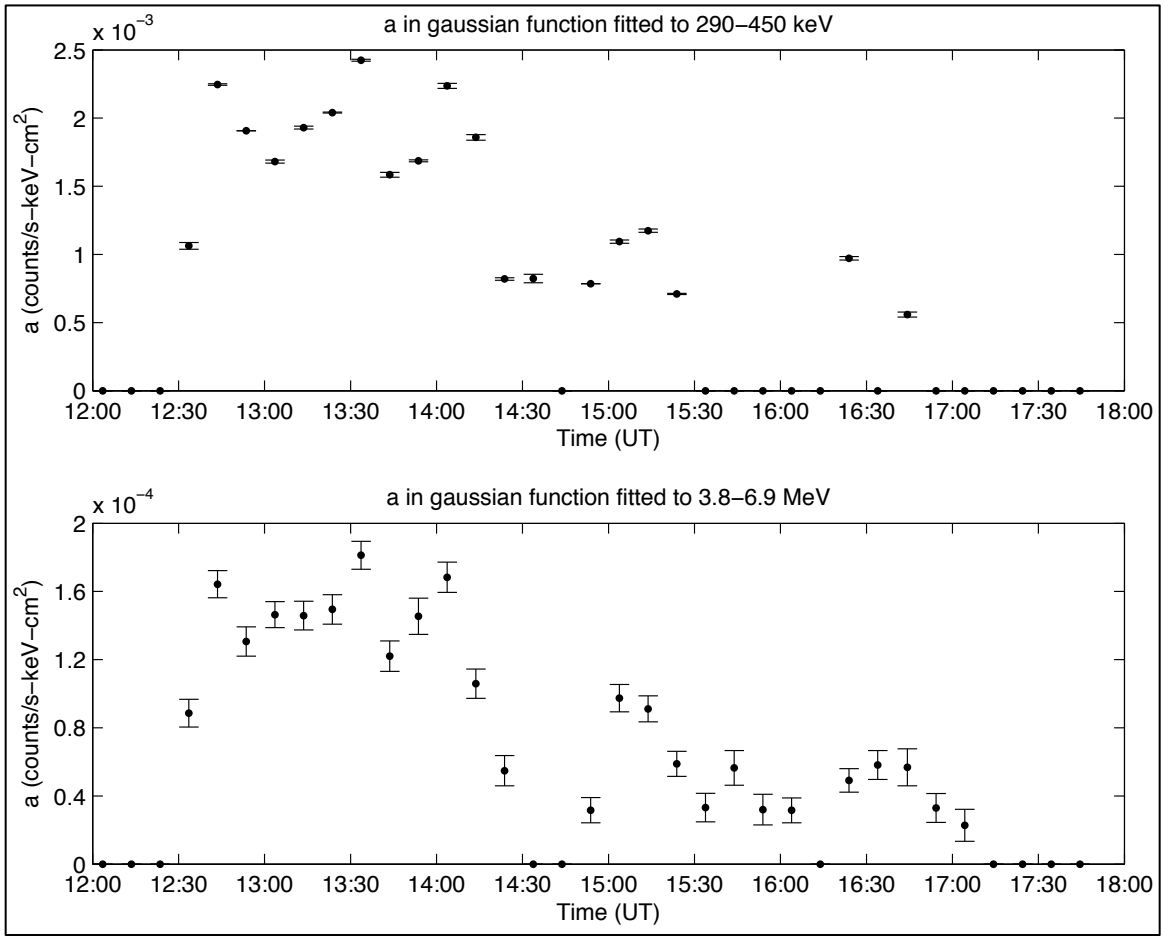

Figure 35. The amplitudes of both Gaussian functions fitted to spectral peaks between 290 – 450 keV and 3.8 – 6.9 MeV.

Spectral peaks have been observed in previous balloon datasets. As was discussed previously, several different spectral peaks were measured during the MINIS campaign as a result of solar energetic particles from a solar flare interacting with the atmosphere [*McCarthy et al.*, 2005]. The MINIS balloon's onboard x-ray detector measured large increases in count rate from precipitation as well as peaks

in count rate from gamma ray emission. (Since possible x-ray energies and possible gamma ray energies overlap, x-ray detectors can measure gamma rays as well.) Gamma ray emission was produced by high-energy protons interactions with the atmosphere. **Figure 36** is an example of a 300-second background-subtracted spectrum from January 17th, 2005.

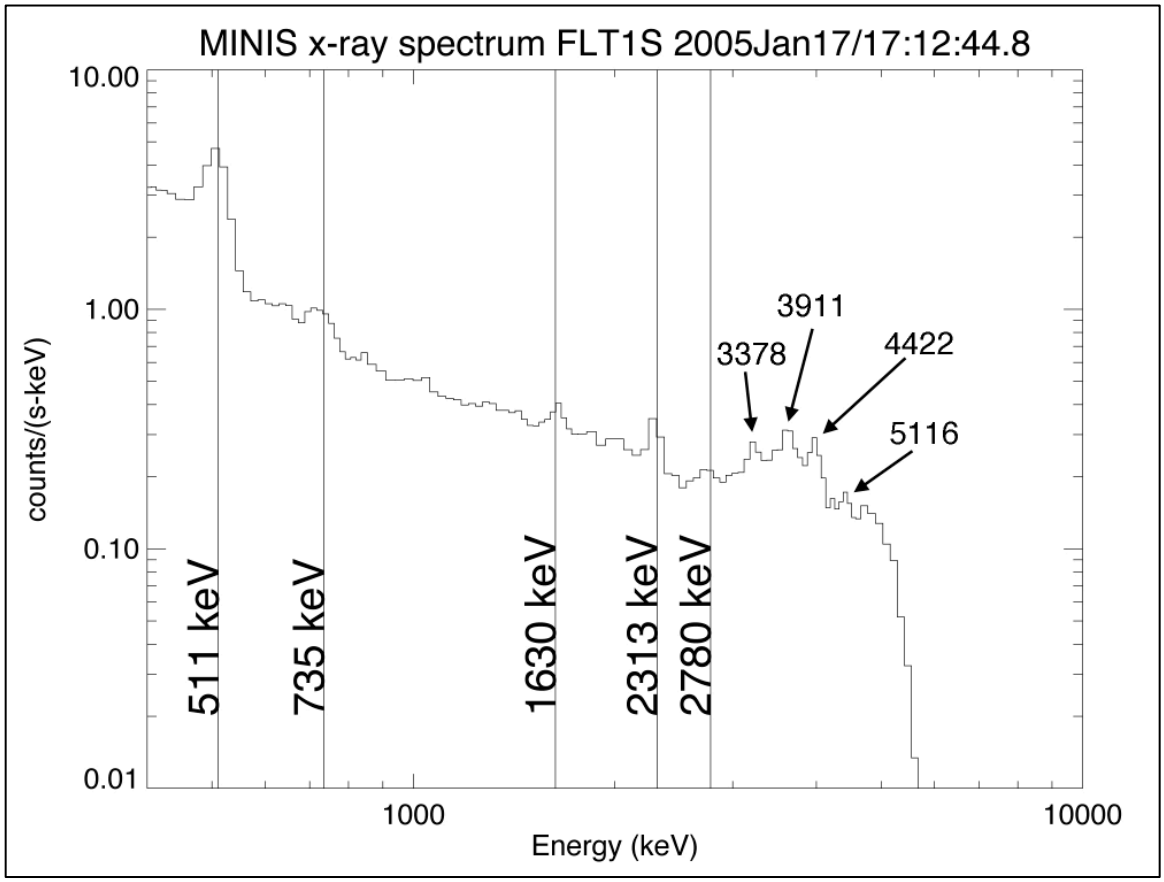

Figure 36. A background-subtracted x-ray spectrum from the MINIS detector during a CME on January 17, 2005 at 17:12 UT. Solid black lines indicate gamma ray emission (excluding the 511 keV line). Arrows point to possible gamma ray emission [*McCarthy et al.,* 2005].

Figure 36 has several noticeable peaks that are labeled by solid black lines and their corresponding energies. (Note that the peak 511 keV has already been

discussed and is always present). This figure also shows several peaks identified by arrows, which are treated separately because temperature corrections were not performed at these energies. *McCarthy et al.* [2005] reported that these peaks are gamma ray emission and correspond to similar peaks observed by the Reuven Ramaty High Energy Solar Spectroscopic Imager (RHESSI). RHESSI is a low-orbiting (600 km altitude) satellite that measures high-energy photons emitted during solar flares like the one on January 17th. **Figure 37** is the background-subtracted spectrum observed by RHESSI at the same time of the MINIS spectrum observed in **Figure 36**.

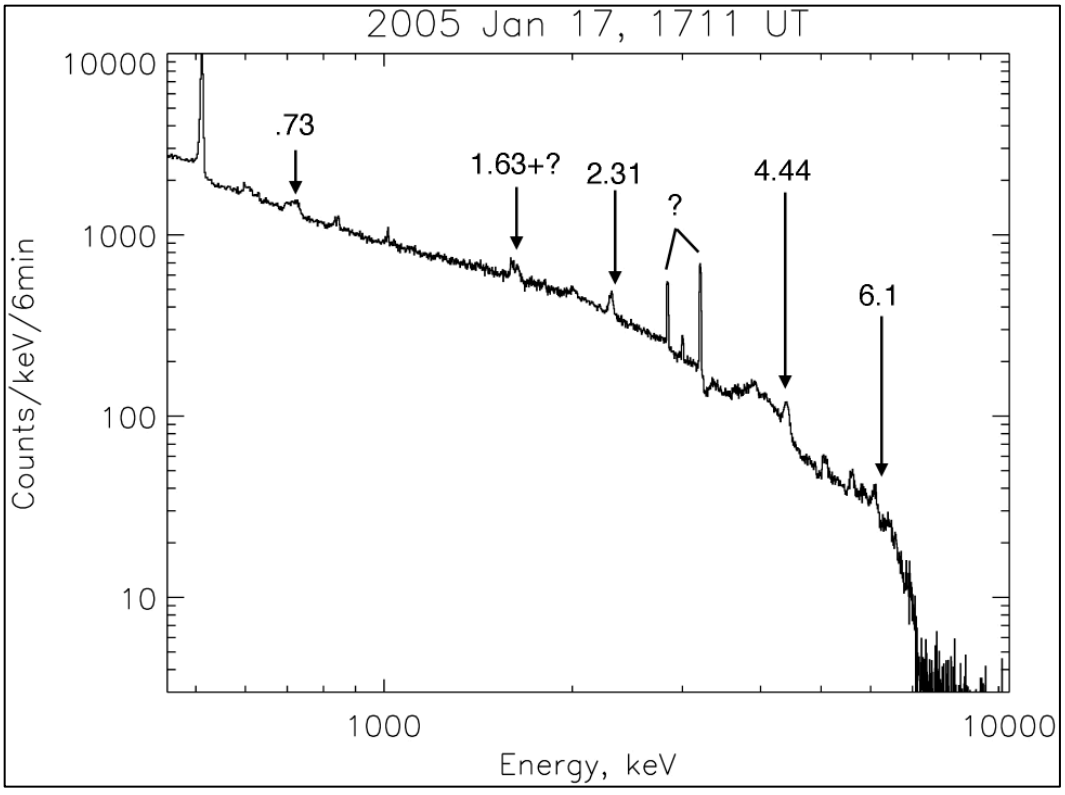

Figure 37. RHESSI observed high-energy photon spectrum during the same CME on January 17, 2005 at 17:11 UT. Arrows point to gamma ray emission that matches MINIS observed spectral peaks. Peaks underneath the question mark are possible instrument artifacts [*McCarthy et al.,* 2005].

There are multiple peaks in the RHESSI data and some have been labeled by arrows that correspond to peaks seen in MINIS, though given in units of MeV, not keV. The peaks around 2 MeV (2000 keV) labeled with a question mark are reported by *McCarthy et al.* as possible instrumental artifacts. Based on this comparison between MINIS and RHESSI, *McCarthy et al*. were able to identify high-energy protons as the source peaks in the balloon x-ray data.

Returning to the Piggyback data under examination, the spectral peaks at 350 keV and 4.8 MeV spectral peaks were compared with observations from MINIS to see if similar peaks occurred in both datasets. If similar peaks were present in both datasets, then the spectral peaks might reasonably be attributed to gamma ray emissions. However, spectral peaks did not occur below 500 keV during the MINIS event, so it is clear that no direct counterpart to BARREL's 350 keV peak exists in MINIS data. MINIS did measure a peak at 4.4 MeV that may have corresponded to the 4.8 MeV BARREL peak because the higher energies in MINIS were not temperature-corrected. However, another look at the RHESSI data confirms that the MINIS peak is indeed at 4.4 MeV. These facts suggest that the BARREL Piggyback detector did not measure the same spectral peaks as MINIS and that high-protons might not have created the spectral peaks seen in the BARREL data.

The Polar Orbiting Environmental Satellite (POES) suite was analyzed to confirm that high-energy protons were not the spectral peak source. The POES fly in a Sun-synchronous low orbit (800 – 850 km altitude) and contain the Space

Environment Monitor (SEM-2) instrument package [*Rodger et al.*, 2010]. The SEM-2 measures energetic particles through several instruments, including the Medium Energy Proton and Electron Detector (MEPED). MEPED observes protons through two detectors that each have six energy channels. The energy ranges covered by these channels are listed in **Table 4**.

Table 4. Precipitating protons are measured in the six different energies by six different channels listed.

MEPED Channel	Energy Range
1	30 – 80 keV
2	80 – 240 keV
3	240 – 800 keV
4	800 – 2500 keV
5	2500 – 6900 keV
6	> 6900 keV

The first MEPED detector, called the 0° detector, points parallel to the Earth-center-to-satellite radial vector. The second detector, called the 90° detector, is oriented perpendicular to the 0° detector. Several studies [*Rodger et al.*, 2010; *Gamble et al*., 2008; *Horne et al*., 2009] have determined that the 0° detector measures the particles that are precipitating into the atmosphere. With this conclusion in mind, proton measurements taken by the 0° detector during the February 14th event were analyzed for comparison with the BARREL spectrum. One of the POES satellites, NOAA-17, flew over the Piggyback balloon at about 12:22 UT and again at about 14:02 UT (marked by black lines). The four highest-energy channels of MEPED proton data are plotted as a function of time in **Figure 38**. (The

first two channels are not plotted because the protons they observe would not have sufficient energy to create either of the spectral peaks being discussed.)

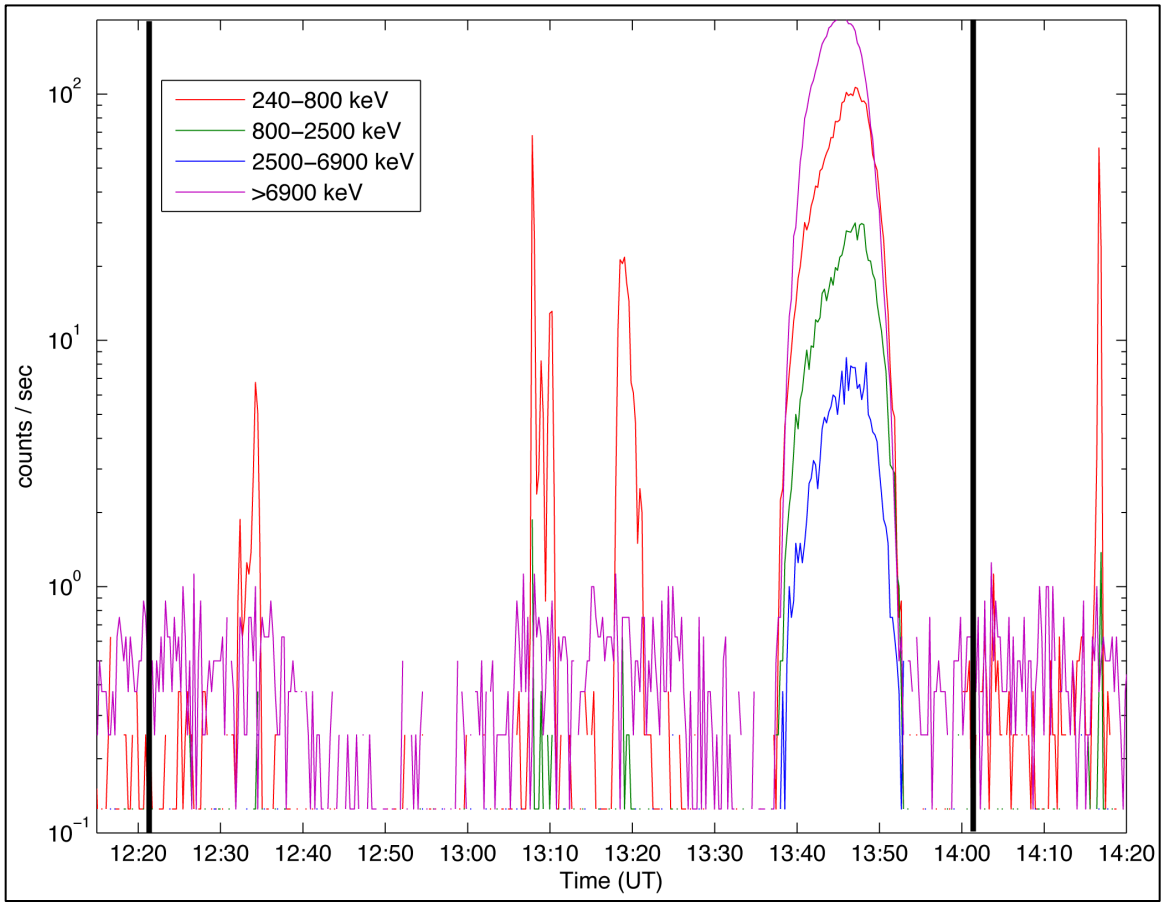

Figure 38. NOAA-17 MEPED proton data of the highest four channels during two conjunctions with the Piggyback balloon. The black lines indicate the conjunctions between POES and the balloon.

The sharp spikes in count rate in the lowest energy channel are a result of the spacecraft passing over the auroral zone and the large increase in all channels around 13:45 UT is the effect of the South Atlantic Anomaly (SAA). However, a close examination of the two conjunctions times at 12:22 UT and 14:02 UT reveals no

increased count rates in any proton channel. These data indicate that there were no highly energetic protons precipitating during the February 14th event, thus the BARREL peaks cannot be attributed to proton activity observed by POES.

Highly energetic protons were eliminated as a source of the BARREL spectral peaks, but it is still unclear what is producing these spectral peaks. It is possible that the peaks could be artifacts of the instrument, but more analysis must be performed to be certain.

Conclusion

The BARREL Piggyback test flight dataset was utilized to investigate the outer radiation belt electron precipitation. The observed x-ray spectra during a large substorm on February 14th were calibrated and background-subtracted to analyze the temporal and spectral characteristics of radiation belt losses during a substorm. The x-ray spectra from 90 keV to 8000 keV were characterized by two functions, an exponential and power law, for lower (90 – 200 keV) and higher energy (1.4 – 8 MeV) parts of spectra. The resulting fit parameters showed that the lower energy activity in the spectra were a result of substorm activity. It was also shown that there were increased counts in the higher energies during the substorm activity.

The parent electron population was estimated for each bremsstrahlung spectrum during the event using a table developed by *Berger and Seltzer* [1972], but extrapolated for electron energies up to 5 MeV for this study. However, the procedure used to calculate the electron spectrum for one spectrum did not yield a unique solution. The possible electron spectra were compared with precipitating electron measurements from SAMPEX in an effort to limit possible solutions, but the comparison was unsuccessful. More complicated models should be employed to gain a more reliable parent electron spectrum.

Two previously unknown spectral peaks were observed in the ten-minute-averaged x-ray spectra at 350 keV and 4.8 MeV. Atmospheric gamma rays produced by high-energy proton interactions were investigated as a possible source using previous research and POES data. However, there is no evidence of increased high-

energy proton precipitation to produce the observed spectral peaks. Other possible sources should be studied and further analysis should be performed on the instruments used in this flight to understand how the artifacts are being produced.

Appendix A – Gain Calibration

Plotting the peak location of the annihilation line in terms of bin number versus scintillator temperature should result in a straight line where a linear equation can be fitted to employ for correcting the gain variation. However, after plotting several quiet days for the Piggyback flight of peak location with respect to temperature, the relationship seemed to change over time. **Figure 39** shows the bin number locations of the 511 peaks for each ten-minute-averaged spectrum with respect to scintillator temperature for three different days from different times of the Piggyback flight.

The cause of this changing relationship could be due to the location of the scintillator temperature sensor. The temperature sensor on payloads built for the second test campaign, which flew in December 2009, were placed at the base of the x-ray detector. The large distance between the sensor and the top of the detector where x-rays are entering could mean the sensor is not accurately tracking the temperature, thus producing variations in the bin number and temperature relationship. The Piggyback payload has not been recovered so that this theory could be confirmed, but in any case, one linear fit could not be established with this dataset.

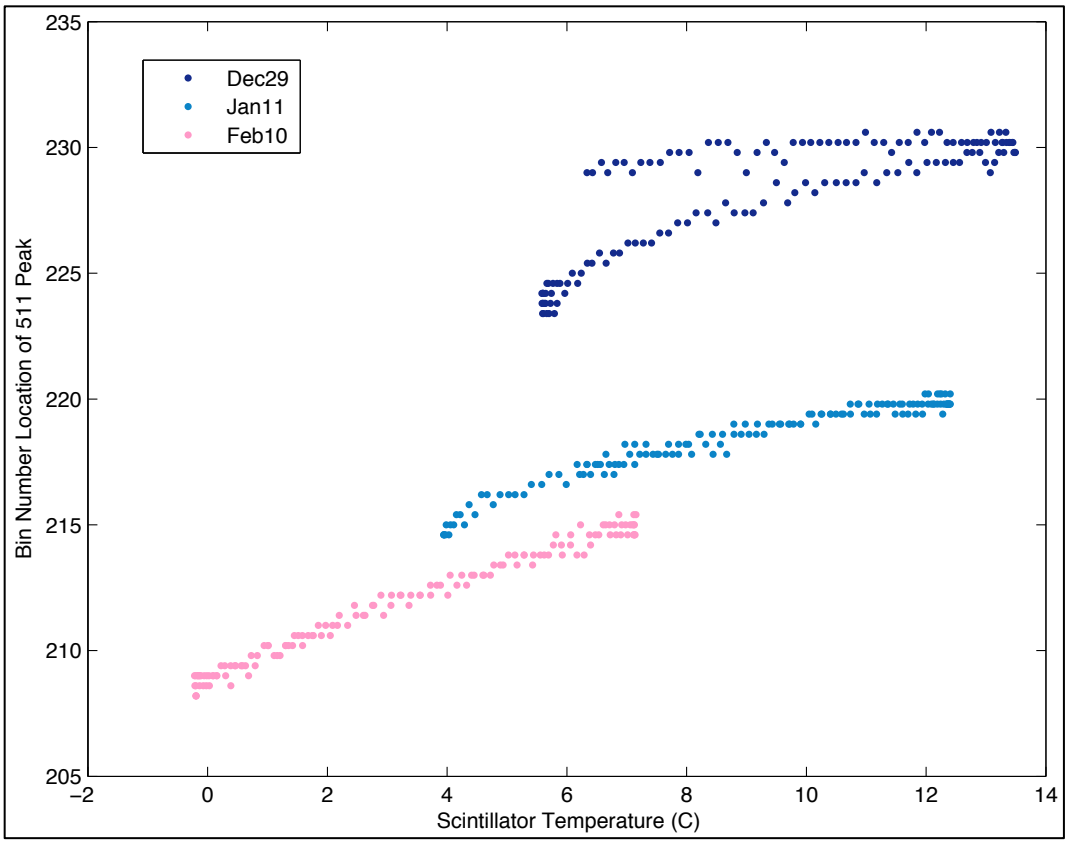

Figure 39. The bin number location of the peak around 511 keV for each spectra on three quiet days as a function of the measured scintillator temperature. The varying relationship could be due to a misplaced temperature sensor.

REFERENCES

Anderson, K. A. and D. C. Enemark (1960), Balloon observations of x rays in the auroral zone II, *J. Geophys. Res., 65*(11), 3521 – 3538.

Angelopolous, V. "THEMIS" SSL Berkeley. July 30, 2010. <http://themis.ssl.berkeley.edu/index.shtml>.

Barcus, J. R. and T. J. Rosenberg (1966), Energy spectrum for auroral-zone x-rays, *J. Geophys. Res., 71*(3), 803 – 823.

Baumjohann, W., and R. A. Treumann (1996). Basic Space Plasma Physics. Imperial College Press, London.

Beisser, K.. "Radiation Belt Storm Probes (RBSP) Web Site". JHU/APL. July 15, 2010 <http://rbsp.jhuapl.edu/index.php>.

Berger, M. J. and S. M. Seltzer (1972), Bremsstrahlung in the atmosphere, *J. Atmos. Terr. Phys., 34*(85).

Bevington, Philip R. and D. Keith Robinson. Data Reduction and Error Analysis for the Physical Sciences. 3rd Ed. New York: McGraw-Hill, 2003.

Bjordal, J., H. Trefall, S. Ullaland, A. Brewersdorff, J. Kangas, P. Tanskanen, G. Fremser, K. H. Saeger, and H. Specht (1971), On the morphology of auroral-zone X-ray events – I : Dynamics of midnight events, *J. Atmos. Terr. Phys., 33*, 605 – 626.

Blake, J. B., M. D. Looper, D. N. Baker, R. Nakamura, B. Klecker, and D. Hovestadt (1996), New high temporal and spatial resolution measurement by SAMPEX of the precipitation of relativistic electrons, *Adv. Space Res. 18*(8).

Brown, R., J. Barcus, and N. Parsons (1965), Balloon observations of auroral zone x rays in conjugate regions. 1. Slow time variations, *J. Geophys. Res., 70*(11), 2579 – 2598.

Cayton, T. E., R. D. Belian, S. P. Gary, T. A. Fritz, D. N. Baker (1989), Energetic electron components at geosynchronous orbit, *Geophys. Res. Lett. 16*, 147.

Chen, Y., G. Reeves, and R. Friedel (2007), The energization of relativistic electrons in the outer Van Allen radiation belt, *Nature Physics*, Vol. 3, Issue 9, 614-617.

Clilverd. M. A., C. J. Rodger, R. M. Millan, J. G. Sample, M. Kokorowski, M. R. McCarthy, T. Ulrich, T. Raita, A. Kavanagh, E. Spanswick (2007), Energetic particle

precipitation into the middle atmosphere triggered by a coronal mass ejection., *J. Geophys. Res.*, *112*, A12206, doi: 10.1029/2007JA012395.

CRC Handbook of Chemistry and Physics, 2009-2010, 90th ed. Edited by David R. Lide, CRC Press: Boca Raton, 2009.

Foat, J. E., R. P. Lin, D. M. Smith, F. Fenrich, R. Millan, I. Roth, K. R. Lorentzen, M. P. McCarthy, G. K. Parks, and J. P. Treilhour (1998), First detection of a terrestrial MeV X-ray burst, *Geophys. Res. Lett. 25*(22), 4109-4112.

Gamble, R. J., C. J. Rodger, M. A. Clilverd, J. A. Sauvaud, N. R. Thomson, S. L. Stewart, R. J. McCormick, M. Parrot, and J.-J. Berthelier (2008), Radiation belt electron precipitation by manmade VLF transmissions, *J. Geophys. Res., 113*, A10211, doi:10.1029/2008JA013369.

Hewitt, J. (2009), BARREL Piggyback test flight observations of energetic electron precipitation, Master's thesis, Dartmouth College.

Holt, S. S. (1970), "X-ray detectors." *Introduction to Experimental Techniques of High-Energy Astrophysics*. Ed. H. Ogelman and J. R. Wayland, Washington, D.C., NASA, 63 – 94.

Horne, R. B., M. M. Lam, and J. C. Green (2009), Energetic electron precipitation from the outer radiation belt during geomagnetic storms, *Geophys. Res. Lett., 36*, L19104, doi:10.1029/2009GL040236.

ICRU (1980), *Radiation Quantities and Units,* Report 33 of the International Commission on Radiation Units and Measurements (Bethesda, MD).

Kaler, James B. Stars. New York: Scientific American Library, 1992.

Kangas, J., L. Lukkari, P. Tanskanen, H. Trefall, J. Stadsnes, G. Kremser, and W. Riedler (1975), On the morphology of auroral-zone X-ray events – IV. Substorm-related electron precipitation in the local morning sector, *J. Atmos. And Terr. Physics 37***,** 1289 – 1303.

Kennel, C. F., and H. E. Petschek (1966), Limit on stably trapped particle fluxes, *J. Geophys. Res. 71*(1), 1 – 28.

Kivelson, M. and C. Russell. Introduction to Space Physics, New York: Cambridge University Press, 1995.

Knoll, Glenn F. Radiation detection and measurement, New York: Wiley, 1979.

Li, X., and M. Temerin (2001), The electron radiation belt, *Space Sci. Rev.* 95(1-

2),569-580.

Makhmutov, V. S., G. A. Bazilevskaya, L. Desorgher, and E. Flückiger (2006), Precipitating electron events in October 2003 as observed in the polar atmosphere, *Adv. Space Res., 38*, 1642 – 1646.

McCarthy et al. (2005), MINIS balloon and RHESSI observations of a solar energetic particle event, AGU Fall Meeting, abstract #SH23A-033.

Meredith, N. P., R. B. Horne, S. A. Glaubert, and R. R. Anderson (2007), Slot region electron loss timescales due to plasmaspheric hiss and lightning-generated whistlers, *J. Geosphys Res. 112*, A08214.

Millan, R. M., Lin, R. P., Smith, D. M., Lorentzen, K. R., and M. P. McCarthy (2002), X-ray observations of MeV electron precipitation with a balloon-borne germanium spectrometer, *Geophys. Res. Lett.*, *29*, 2194, doi: 10.1029/2002GL015922.

Millan, R.M. and R. M. Thorne (2007), Review of radiation belt relativistic electron losses, *Jour. Atmos. Solar-Terr. Phys.* 69, 362-377.

Parks, G. K., C. Gurgiolo, and R. West (1979), Relativistic electron precipitation, *Geophys. Res. Lett. 6*(5), 393 – 396.

Reeves, G. D., K. L. McAdams, R. H. W. Friedel, T. P. O'Brien (2003), Accelerations and loss of relativistic electrons during geomagnetic storms. *Geophys. Res. Lett. 30*, 1529, doi:10.1029/2002GL016513.

Rodger, C. J., M. A. Clilverd, J. C. Green, and M. M. Lam (2010), Use of POES SEM-2 observations to examine radiation belt dynamics and energetic electron precipitation into the atmosphere, *J. Geophys. Res. 115*, A04202, doi:10.1029/2008JA014023.

Smith, D. M., R. P. Lin, K. A. Anderson, K. Hurley, and C.M. Johns (1995), High-resolution spectra of 20-300 keV hard x-rays from electron precipitation over Antarctica, *J. Geophys. Res. 100*(A10), 19, 675-19, 685.

Tysganenko, N. A. (1989), A magnetosperhic magnetic field model with a warped tail current sheet, *Planet. Space Sci.*, 37(1), 5-20.

Van Allen, James A. Origins of Magnetospheric Physics, Washington D.C. :Smithsonian Institution Press, 1983.

Winckler, J. R., L. Peterson, R. Arnoldy, and R. Hoffman (1958), X-rays from visible aurorae at Minneapolis*, Phys. Rev.*, 110, 1221.